

# A COMETARY BOW SHOCK AND MID-INFRARED EMISSION VARIATIONS REVEALED IN *SPITZER* OBSERVATIONS OF HD 34078 AND IC 405<sup>1</sup>

KEVIN FRANCE<sup>2</sup>, STEPHAN R. MCCANDLISS, AND ROXANA E. LUPU

Department of Physics and Astronomy, Johns Hopkins University,  
3400 N. Charles Street, Baltimore, MD 21218

(Received 2006 August 31; Revised 2006 October 18; Accepted 2006 October 27)  
*To appear in the Astrophysical Journal*

## ABSTRACT

We present new infrared observations of the emission/reflection nebula IC 405 obtained with the *Spitzer Space Telescope*. Infrared images in the four IRAC bands (3.6, 4.5, 5.8, and 8.0  $\mu\text{m}$ ) and two MIPS bands (24 and 70  $\mu\text{m}$ ) are complemented by IRS spectroscopy (5 – 30  $\mu\text{m}$ ) of two nebular filaments. The IRAC (8.0  $\mu\text{m}$ ) and MIPS imaging shows evidence of a bow shock associated with the runaway O9.5V star, HD 34078, created by the interaction between the star and nebular material. The ratio of emission at 24 to 70  $\mu\text{m}$  is higher in the immediate vicinity of HD 34078 than in the outer filaments, providing evidence for elevated dust temperatures ( $T_d \gtrsim 90$  K) in the shock region. The nebular imaging reveals that the morphology is band dependent, with varying contributions from aromatic emission features, H<sub>2</sub>, and dust emission. Nebular spectroscopy is used to quantify these contributions, showing several aromatic emission bands between 6 – 14  $\mu\text{m}$ , the S(5), S(3), S(2), and S(1) pure rotational emission lines of H<sub>2</sub>, and atomic fine structure lines of Ne, S, and Ar. The low-dispersion spectra provide constraints on the ionization state of the large molecules responsible for the aromatic infrared features. H<sub>2</sub> rotational temperatures of the two bright nebular filaments are determined from the observed line strengths. An average  $T(\text{H}_2) \sim 400$  K is inferred, with evidence for additional non-uniform excitation by UV photons in the intense radiation field of HD 34078. The photoexcitation hypothesis is supported by direct measurement of the far-UV H<sub>2</sub> fluorescence spectrum, obtained with *FUSE*.

*Subject headings:* dust — ISM: molecules — ISM: individual (IC 405) — reflection nebulae — Infrared: ISM

## 1. INTRODUCTION

IC 405 is an emission/reflection nebula in Auriga (Herbig 1958, 1999). It is illuminated by the O9.5V star HD 34078 (AE Aur,  $V = 6.0$ ), a high proper motion ( $\approx 40$  mas/yr; Blaauw & Morgan 1954) runaway star ejected from the Orion star-forming region in a binary-binary interaction approximately 2.5 million years ago (Bagnuolo et al. 2001). The star and the optical nebula are roughly cospatial at present (Herbig 1958; France et al. 2004; Boissé et al. 2005), at a distance of 450 pc. The sightline to HD 34078 is considerably reddened ( $E(B - V) = 0.53$ ; Cardelli et al. 1989), however, the extended nebular regions appear to be free of foreground attenuation (France et al. 2004).

The large transverse velocity of the star indicates that it has only recently encountered the nebular material with which it now interacts. The present geometric configuration has made the HD 34078 sightline a target for studies of interstellar absorption line variation. Herbig (1999) combines fifty years of atomic and molecular line observations in the violet-blue ( $\lambda 3400 - 4900$  Å) to set an upper limit on the length scale of substructure in the ISM of 1450 AU. More recently, variations in the column density of interstellar CH and CN

(10 – 20 %) have been observed on this sightline, setting a smaller upper limit on the substructure size ( $\leq 200$  AU) towards HD 34078 (Rollinde et al. 2003). A similar study (Boissé et al. 2005) using *Far Ultraviolet Spectroscopic Explorer* (*FUSE*) observations has set an upper limit on the molecular hydrogen (H<sub>2</sub>) column variation of  $\leq 5\%$ , constraining the scale to a few tens of AU. They also find evidence for interaction between HD 34078 and the surrounding nebula. Detections of excited molecular hydrogen absorption lines (measurements up to  $v = 0$ ,  $J = 11$  and tentative detections up to the  $v = 2$  level) are evidence for fluorescent pumping by the local stellar UV field (Boissé et al. 2005). Additional observations of the interaction between the UV radiation field of HD 34078 and the nebular gas and dust are presented by France et al. (2004). They present a spectroscopic study of far-UV dust scattering and fluorescent H<sub>2</sub> emission lines in the nebula.

Evidence for interaction between the star and nebular dust grains has also been detected by *IRAS* (van Buren et al. 1995). The high proper motion of HD 34078 makes it a candidate host for a bow shock. As a massive star moves supersonically through an ambient interstellar medium, stellar radiation pressure and/or strong stellar winds can produce a comet-shaped, compact H II region surrounded by shocked molecular gas (van Buren & McCray 1988; van Buren et al. 1990). A 60  $\mu\text{m}$  excess observed in *IRAS* maps (van Buren et al. 1995; Noriega-Crespo et al. 1997) identifies IC 405 as a potential bow shock region.

<sup>1</sup> Based in part on observations made with the the *Spitzer Space Telescope*, which is operated by the Jet Propulsion Laboratory, California Institute of Technology, under a contract with NASA.

<sup>2</sup> Current Address: Canadian Institute for Theoretical Astrophysics, University of Toronto, 60 St. George Street, Toronto, ON M5S 3H8

In this paper, we present the first direct imaging of the bow shock around HD 34078 with the *Spitzer Space Telescope*-IRAC and MIPS. We also use MIPS data to study the nebular dust emission, characterize the spectroscopic properties of aromatic emission features (AEFs) and  $H_2$  using nebular observations made with the *Spitzer*-IRS, and put these new observations in context with existing studies of IC 405. §1.1 provides background information on the diagnostic properties of AEFs,  $H_2$ , and dust in diffuse nebulae. In §2, we describe the new *Spitzer* data, and introduce supporting far-UV spectroscopy from *FUSE*. An analysis of the infrared (IR) imaging and spectroscopy is given in §3. In §4, we discuss the structure of the bow shock region, present determinations of the  $H_2$  rotational and dust temperatures, and analyze spatial variations in AEF carrier ionization across the nebular filaments. Our findings and a summary of the observations are presented in §5.

### 1.1. AEFs, $H_2$ , and Dust Emission in Photodissociation Regions

AEFs have been found to be ubiquitous in the mid-IR spectra (3 – 20  $\mu\text{m}$ ) of reflection nebulae and H II regions (see van Dishoeck 2004 for a recent review). AEFs are seen as broad bands in the *ISO-SWS/ISO-CAM-CVF* and *Spitzer*-IRS wavelength ranges, with lines complexes centered on 3.3, 6.2, 7.7, 8.6, 11.2, and 12.7  $\mu\text{m}$ . These features are usually attributed to a superposition of C – C and C – H vibrational modes in a distribution of polycyclic aromatic hydrocarbons (PAHs) consisting of tens to hundreds of C-atoms (Schutte et al. 1993; van Dishoeck 2004). However, discrepancies between astronomical emission features and laboratory PAH spectra exist, preventing a conclusive identification of the exact carrier of the AEFs (Gordon et al. 2006 and references therein). The carrier population that gives rise to the observed mid-IR bands (also called Aromatic Infrared Bands; Verstraete et al., 2001) spans a range of sizes and ionization states. The size distribution is thought to be regulated by the hardness of the illuminating radiation field (Verstraete et al. 2001) while the aromatic molecule ionization balance is controlled by the strength of the ultraviolet (UV) radiation field and the electron density (Bakes et al. 2001; Bregman & Temi 2005). The relative strengths and spectral profiles of the major AEFs reflect the physical state of the carrier population in a given environment.

Variations in the spectral features of the AEFs can be used to quantify the response of the carrier molecules to different radiation and density environments (Bakes et al. 2001). These variations can be studied by comparing a sample of nebulae (Verstraete et al. 2001), at different locations within a single object (Verstraete et al. 1996; Hony et al. 2001), or in the diffuse interstellar medium (Boulanger et al. 2000). The C – H emission features at 3.3 and 11.2  $\mu\text{m}$  are found to be well correlated over a range of physical conditions, however the relative strengths of the C – H and C – C features are observed to vary with environment (Hony et al. 2001; van Dishoeck 2004). The ratio of a C – C to a C – H feature (6.2/11.2  $\mu\text{m}$  for example) reflects the ionization state as C – C band strengths are stronger in ionized aromatic carriers while C – H bands display the opposite behavior (Uchida et al. 2000). The increase in the

6.2  $\mu\text{m}$  C – C feature (and more generally, the 6.2, 7.7, and 8.6  $\mu\text{m}$  bands) is due to the dipole moment produced by a change in charge distribution during ionization (Peeters et al. 2002). The carriers of the AEFs fall in the middle of the molecular mass distribution in reflection nebulae and H II regions (which we will group under the broad heading of photodissociation regions; PDRs).

$H_2$ , residing at the lower limit of this distribution, makes up the majority of the molecular mass in these objects (Hollenbach & Tielens 1997; Shaw et al. 2005).  $H_2$  is seen to emit from far-UV to the mid-IR wavelengths, excited by both UV photons (i.e. - fluorescence) and thermal processes, such as collisions and shocks. Detection of the UV emission lines of  $H_2$  is one clear indication of photoexcitation.  $H_2$  dissociates in environments with temperatures corresponding to the excited electronic levels that give rise to the UV lines (Shull & Beckwith 1982). The emission nebula IC 63 is the prototypical object for PDR studies of fluorescent  $H_2$ . The far-UV spectrum has been well-studied (Witt et al. 1989; Hurwitz 1998; France et al. 2005), confirming stellar continuum photons as the excitation source of the observed emission. Far-UV  $H_2$  emission lines in IC 405 have been observed (France et al. 2004), and these observations will be discussed below.

Near-IR observations of the rovibrational emission lines of  $H_2$  can also be used to constrain the molecular excitation mechanism. Collisional processes can populate the lowest excited vibrational states of the molecule ( $v = 1$  and 2), but the fluorescent cascade associated with the electronic excitation of  $H_2$  by UV photons is the only mechanism (ignoring excitation by non-thermal electrons) available to populate higher vibrational states ( $v > 2$ ) as the molecules dissociate at kinetic temperatures proportional to these higher vibrational levels (Shull & Beckwith 1982). Ratios of these excited vibrational states can be compared with model predictions to determine the excitation mechanism (Black & van Dishoeck 1987). Near-IR line ratios indicate UV excitation in IC 63 (Luhman et al. 1997), the bright reflection nebulae NGC 2023 and NGC 7023 (Martini et al. 1999; Takami et al. 2000), and on larger scales in molecular clouds (Luhman & Jaffe 1996). Collisions contribute to the rovibrational excitation of  $H_2$  in dense molecular clouds (Kristensen et al. 2003) and regions where shocks play an important role, such as planetary nebulae (Kastner et al. 1996; Lupu et al. 2006). The pure rotational emission lines of  $H_2$ , accessible only in the mid-IR, give diagnostic information about the molecular gas temperature in PDRs. Ratios of these lines have been used to derive temperatures in star-forming regions (Rosenthal et al. 2000; Allers et al. 2005), PDRs (Thi et al. 1999; Habart et al. 2004), and external galaxies (Valentijn & van der Werf 1999; Armus et al. 2004).

Dust grains populate the upper end of the molecular mass distribution in PDRs. Grains are observed through their thermal emission in the mid/far-IR (Schnee et al. 2005 and references therein) and in the attenuation and scattering of ultraviolet and visible photons (Cardelli et al. 1989; Witt et al. 1993; Burgh et al. 2002; Draine 2003). *IRAS* observations of PDRs find that grain emission is spatially correlated with near-IR  $H_2$  emission (Luhman & Jaffe 1996). Jansen et al. (1994,

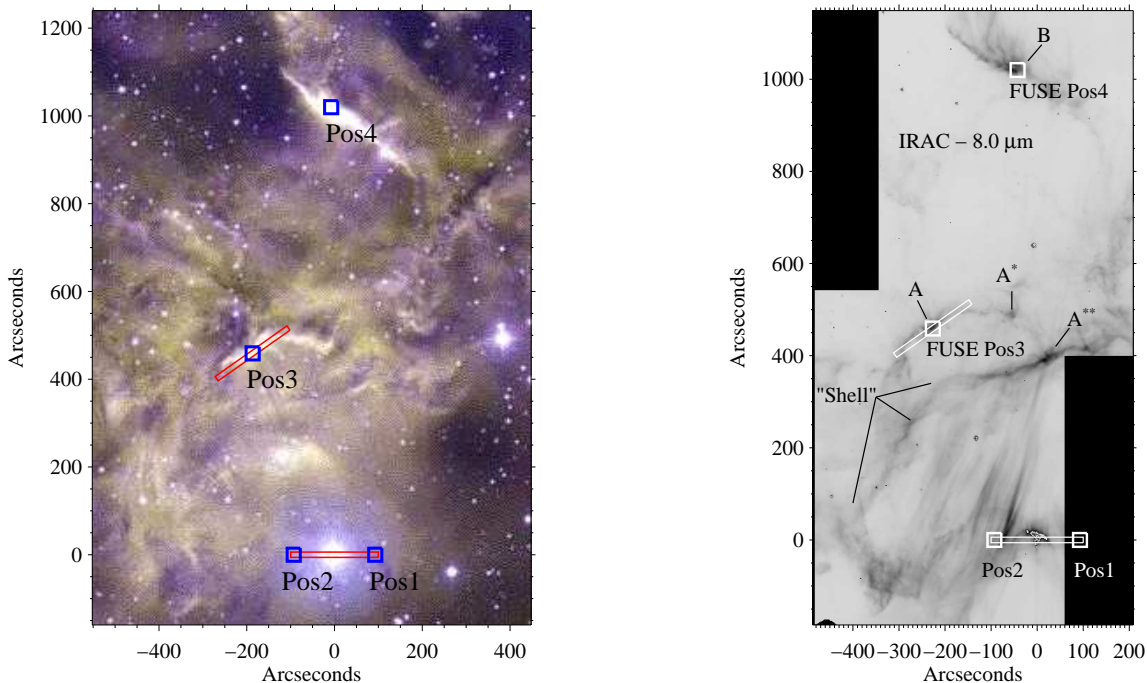


FIG. 1.— *Left*: Optical image of IC 405 from France et al. (2004). *Right*: Post-BCD 8.0  $\mu\text{m}$  IRAC images of IC 405, scaled to highlight the rich nebular structure. The origin is the position of the illuminating, runaway O9.5 star, HD 34078. The main nebular regions studied in this work are labeled A and B. White overlays represent far-UV spectrograph apertures (the squares are the *FUSE* LWRS slit and the rectangles represent a rocket-borne spectrograph; France et al. 2004). At the cores of the bright filaments, discrete features contribute  $\leq 40\%$  of the nebular emission at 8  $\mu\text{m}$ .

1995) present observations of IC 63, where dust emission is coincident with the region of peak  $\text{H}_2$  emission (at UV and IR wavelengths) as well as CO and other molecules. This correlation would be expected as dust grains are thought to be the primary site of  $\text{H}_2$  formation in the interstellar medium (Cazaux & Tielens 2002, 2004). Additionally, photoelectric emission from small grains is an important source of heating in PDRs (Abel et al. 2005). Habart et al. (2004) provide observational evidence for a correlation between AEFs and  $\text{H}_2$ , which they propose is related to  $\text{H}_2$  formation on PAHs. With the wealth of observational evidence that these molecules are interrelated in PDRs, it follows naturally to study this group as a whole.

In this work, we further address the physical conditions of the AEF carriers and their relationship with  $\text{H}_2$  and dust grains by presenting new observations of the emission/reflection nebula IC 405 made with *Spitzer*. We use a combination of imaging and spectroscopy to constrain the variation in aromatic carrier properties with changing radiation and dust environment through the nebula. Our aim is to present new IR observational characteristics of large molecules, dust grains, and  $\text{H}_2$  in the unique PDR environment of IC 405, for comparison with previous far-UV observations.

## 2. OBSERVATIONS

### 2.1. *Spitzer*

*Spitzer* observations of IC 405 (Program ID 20434) were made at positions coincident with the UV data pre-

sented in France et al. (2004), where  $\text{H}_2$  fluorescence was observed above the level of dust scattered light (*FUSE* Pos3: RA =  $5^{\text{h}}16^{\text{m}}30.21^{\text{s}}$ ,  $\delta = +34^{\circ}24'56.4''$  and *FUSE* Pos4: RA =  $5^{\text{h}}16^{\text{m}}18.64^{\text{s}}$ ,  $\delta = +34^{\circ}32'25.2''$ , J2000; see also §2.2). The Infrared Array Camera (IRAC) observed the nebula in mapping mode on 2005 September 23, with an exposure time of 12 seconds per frame, for a total integration time approximately 825 seconds. Details of the IRAC instrument can be found in Fazio et al. (2004). The IRAC pointings covered the northern nebula in all four bands (r16033792), with the 4.5/8.0  $\mu\text{m}$  channel acquiring data of HD 34078 and the associated bow shock (r16033280, Figure 1). The images were reduced with the data processing pipeline (S14.0.0) provided by the *Spitzer Science Center* (SSC). Analysis was performed on the post-Basic Calibrated Data (BCD) products.

Using the mapping mode on the Infrared Spectrograph (IRS, Houck et al. 2004), we obtained spectra clustered around previous *FUSE* observations Pos3 (r16033024) and Pos4 (r16033536). IRS programs were carried out on 2006 March 17 and 19 with a total exposure time of  $\sim 9600$  seconds. Data at all IRS wavelengths were acquired through both the high and low-resolution apertures (SL, SH, LL, and LH). The spatial coverage of the low-resolution aperture scan allows us to correlate spectral variations with nebular morphology, hence this work will focus on an analysis of the low-resolution (Short-Low, 5 – 15  $\mu\text{m}$ ;  $R = 60 - 130$ ) data. Short-High and Long-Low spectroscopic data were used as supporting observations. The post-BCD (pipeline version S13.2.0)

TABLE 1  
MID AND FAR-IR PHOTOMETRY OF BOW SHOCK REGION.

| Position       | RA (2000) <sup>a</sup><br>( <sup>h</sup> <sup>m</sup> <sup>s</sup> ) | $\delta$ (2000)<br>( <sup>°</sup> <sup>'</sup> <sup>''</sup> ) | F <sub>8</sub><br>(Jy) | F <sub>24</sub><br>(Jy) | F <sub>70</sub><br>(Jy) | T <sub>d</sub> <sup>b</sup><br>(K) |
|----------------|--|--|------------------------|-------------------------|-------------------------|------------------------------------|
| S <sub>E</sub> | 05 16 20.98  | +34 18 52  | 0.508 ± 0.083          | 3.435 ± 0.229           | 1.945 ± 0.169           | 83.93 ± 2.06                       |
| S <sub>C</sub> | 05 16 18.42  | +34 18 58  | 0.805 ± 0.103          | 4.286 ± 0.255           | 1.904 ± 0.167           | 88.76 ± 2.24                       |
| S <sub>W</sub> | 05 16 16.83  | +34 18 48  | 0.675 ± 0.094          | 3.347 ± 0.225           | 1.805 ± 0.162           | 84.85 ± 2.16                       |

<sup>a</sup>Shock pointings were defined from analysis of the 24  $\mu\text{m}$  MIPS data obtained near HD 34078.

<sup>b</sup>Dust temperatures were derived from the ratio of 24 to 70  $\mu\text{m}$  flux density, F<sub>24</sub>/F<sub>70</sub>. This temperature should be considered a lower limit due to the saturation of the 24  $\mu\text{m}$  map.

reduced one-dimensional spectra were tagged according to the central aperture position for registration with the associated filaments observed in the imaging. As the “on-filament” nebular positions filled most of the Short-Low aperture, analyzing the full-slit extraction at all pointings yielded information about both the spectral characteristics and the slit-filling fraction.

We also obtained mosaic maps of IC 405 in the three bands of the Multiband Imaging Photometer for *Spitzer* (MIPS). A description of the MIPS instrument is given in Rieke et al. (2004). The data (r16032768) were obtained on 2006 February 28. The post-BCD scan maps (S13.2.0) at 24 and 70  $\mu\text{m}$  (Figures 2 and 3) were used to perform photometry of several nebular filaments and complement the imaging at shorter wavelengths. The 24 and 70  $\mu\text{m}$  maps are of high quality, but we note the inner 10 – 25'' of the bow shock region near HD 34078 is likely saturated on the 24  $\mu\text{m}$  Si:As array. The 160  $\mu\text{m}$  map contains gaps that make measuring long-wavelength photometry very challenging, we will focus on the shorter wavelength MIPS channels here. The 24 and 70  $\mu\text{m}$  scans covers roughly 8' × 54' and 5' × 52', respectively, both centered on *FUSE* Pos4.

## 2.2. FUSE

IC 405 was observed by *FUSE* on 2003 March 11 – 13 as part of the D127 guest observer program (France et al. 2004). Spectroscopy was obtained in the *FUSE* far-UV bandpass (905 – 1187 Å) through the low-resolution (30'' × 30'';  $\Delta\lambda \approx 0.33\text{\AA}$ ) aperture (Moos et al. 2000). The data acquired at positions Pos3 and Pos4 show H<sub>2</sub> emission lines and were used to guide the *Spitzer* observations presented in this work. We use the LiF2a (1087 – 1179Å) channel to measure the strength of the strongest far-UV band of continuum pumped H<sub>2</sub> fluorescence,  $\lambda \sim 1100\text{\AA}$ , for comparison with the pure rotational emission lines in the IRS bandpass (§4.2). The *FUSE* data were obtained in time-tagged mode and reduced with the CalFUSE pipeline, version 2.2.3, with errors determined from the associated count rate plots. Both positions were observed for roughly 12.5 ksec.

## 3. ANALYSIS AND RESULTS: IMAGING AND SPECTROSCOPY

The 8.0  $\mu\text{m}$  IRAC images showed the best combination of S/N ( $\sim 6 - 38$  for the faintest to the brightest nebular features), spatial resolution ( $\lesssim 2''$ ; Fazio et al. 2004), and nebular structure with a field-of-view that covered all of

TABLE 2  
8  $\mu\text{m}$  IRAC PHOTOMETRY OF NEBULAR FILAMENTS.

| Position | Program   | RA (2000)<br>( <sup>h</sup> <sup>m</sup> <sup>s</sup> ) | $\delta$ (2000)<br>( <sup>°</sup> <sup>'</sup> <sup>''</sup> ) | Flux <sup>a</sup><br>(Jy) |
|----------|-----------|---|--|---------------------------|
| A        | r16033280 | 05 16 30.97   | +34 25 04  | 0.466 ± 0.079             |
| A*       | r16033280 | 05 16 19.84   | +34 25 18  | 0.385 ± 0.072             |
| A**      | r16033280 | 05 16 15.53   | +34 23 57  | 0.573 ± 0.088             |
| B        | r16033792 | 05 16 16.88   | +34 32 21  | 0.543 ± 0.085             |

<sup>a</sup>The 8.0  $\mu\text{m}$  images contain contributions from AEFs, H<sub>2</sub>, and [Ar II]. The 7.7 AEF contributes between 30 – 40% of the 8.0  $\mu\text{m}$  band flux in the region of peak filament brightness.

the subregions of interest. A composite of the 8.0  $\mu\text{m}$  images is shown in Figure 1. These data provided a reference frame for all of the image and spectroscopic analysis described below. The overall morphology of the 8.0  $\mu\text{m}$  images shows the brightest structures seen in the three-color optical image<sup>3</sup>, displayed in Figure 1 for comparison with the IRAC data. The “shell” structure seen to the East/Northeast of HD 34078 with a radius of  $\sim 400''$  observed in DSS images and in Plate IV of Herbig (1958) is observed at 8.0  $\mu\text{m}$ .

Two bright nebular regions were chosen for analysis in this work, based on previous ultraviolet studies. Filaments A and B were part of the France et al. (2004) far-UV study of IC 405. Data acquired at these positions showed a combination of fluorescent H<sub>2</sub> emission and dust-scattered starlight. These observations provided detection of continuum pumped H<sub>2</sub> emission where the rotational substructure was spectroscopically resolved at wavelengths shortward of Ly $\alpha$ . Filament A is broken up into three subregions: the main A knot with existing UV spectroscopy;  $\sim 175''$  to the west, Filament A\* is a clumpy feature located at the end of the Filament A structure; and Filament A\*\* to the southwest was the brightest feature in the 70  $\mu\text{m}$  data (these nebular features are labeled in Figure 1). The brightest features in the optical image are related to the regions containing Filaments A and B at infrared wavelengths. Filaments A and B are also the dominant features in the 6300 –

<sup>3</sup> T.A. Rector, <http://antwrp.gsfc.nasa.gov/apod/ap011204.html>; also presented in Figure 1 of France et al. (2004).

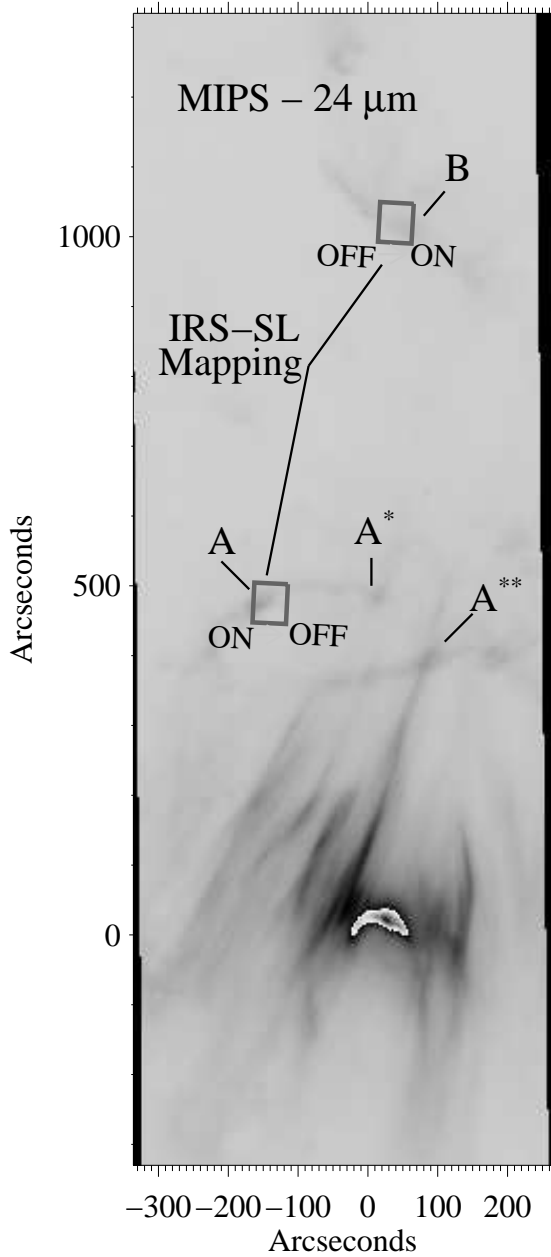


FIG. 2.— Post-BCD 24  $\mu\text{m}$  map of IC 405. The region near HD 34078 (0,0) shows the wake-like morphology, suggesting the presence of a bow shock as the star traverses the ambient nebular material. The bow shock region at 8 and 24  $\mu\text{m}$  can be seen enlarged in Figures 4 and 5. The overlays on Filament A and B represent the IRS-SL scan regions, with the ON/OFF convention used in Figures 10 and 12 indicated. (The IRS-SL scans are shown in more detail in Figures 8 and 9.)

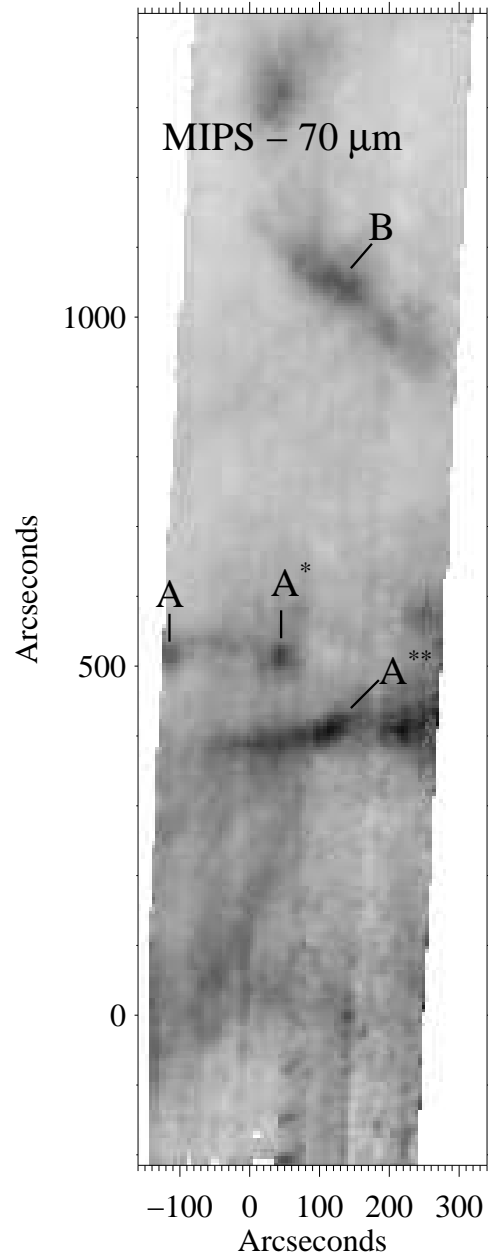


FIG. 3.— Post-BCD 70  $\mu\text{m}$  scan of IC 405. The position of HD 34078 is at the origin. The Filament A\*\* region is the strongest feature in the 70  $\mu\text{m}$  data.

6750  $\text{\AA}$  photographic images presented in Herbig (1958; Plate III), where line emission from  $\text{H}\alpha$ ,  $[\text{N II}]$ , and  $[\text{S II}]$  is the primary source of the nebular brightness.

The following subsections are divided into imaging and spectroscopic results. The imaging is presented first, starting near HD 34078 and moving out into the northern filaments. An analysis of the IRS spectroscopy fol-

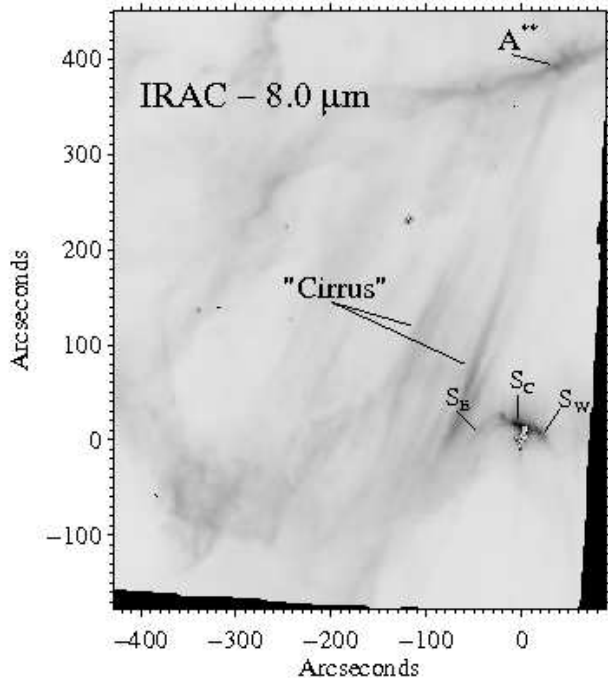


FIG. 4.— IRAC 8.0  $\mu\text{m}$  blow up of the bow shock region, scaled to illustrate the shock structure. The shock subregions are labeled Shock-East ( $S_E$ ), Shock-Center ( $S_C$ ), and Shock-West ( $S_W$ ). Photometry of the subregions is given in Table 1.

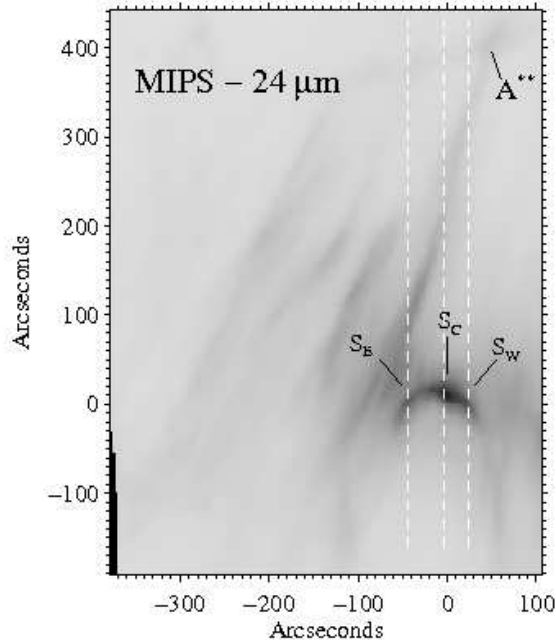


FIG. 5.— MIPS 24  $\mu\text{m}$  blow up of the shock region, scaled to illustrate the shock structure. The stellar position is at the origin. The inner 10 – 25'' near HD 34078 in the direction of stellar motion (North,  $+y$ ) is saturated at 24  $\mu\text{m}$ , indicative of the high temperature of the grains in the shock region. The dashed lines indicate the location and direction of the spatial profiles presented in Figure 7. 24  $\mu\text{m}$  photometry of the shock region is given in Table 1

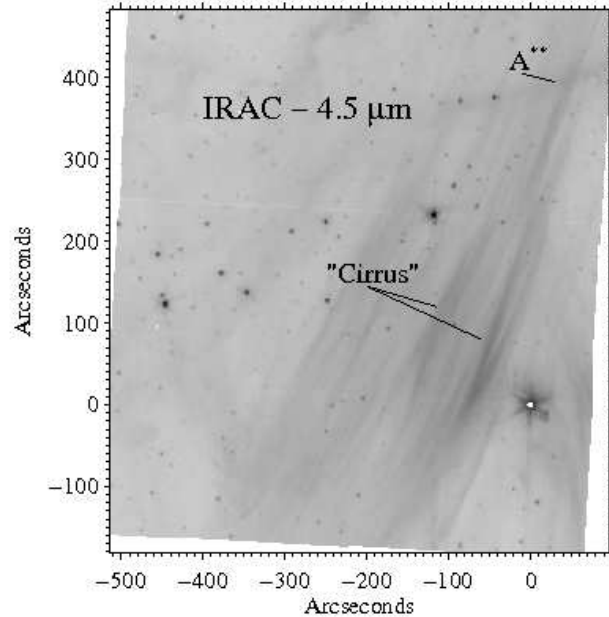


FIG. 6.— IRAC 4.5  $\mu\text{m}$  image of the HD 34078 region with a logarithmic intensity scale to enhance the nebular emission. The “cirrus” features described in §3.1 are identified. The 4.5  $\mu\text{m}$  band shows these structures at a higher contrast than the shell structure seen in Figure 1.

lows, we determine the relative contribution of the nebular species to the IRAC images and observe position-dependent line strengths. We note that the IRAC band overlap regions and spectroscopic programs were centered on Filaments A and B, thus six-band imaging and spectroscopy do not exist for all IC 405 subregions. A brief comparison between the imaging and spectroscopy of the different regions is given in §3.3.

### 3.1. Imaging: IRAC and MIPS

*Bow Shock* - The wake feature seen clearly in the 8.0  $\mu\text{m}$  IRAC (Figure 4) and 24  $\mu\text{m}$  MIPS (Figure 5) images is thought to be enhanced dust emission produced by the interaction of HD 34078 with the ambient nebular medium (van Buren & McCray 1988). The bullet-tip interaction region is seen most clearly in the 24  $\mu\text{m}$  images (despite the saturation of the brightest ridge), and three positions were chosen for analysis. Moving from left to right on the image blow-ups, they are labeled Shock-East ( $S_E$ ), Shock-Center ( $S_C$ ), and Shock-West ( $S_W$ ). The 8.0  $\mu\text{m}$  data show an emission arc of diameter  $\sim 75''$  with an enhancement of factors of  $> 5$  (in units of  $\text{MJy sr}^{-1}$ ) relative to the interfilament medium. The emission arc has a brightness peak 10 – 20'' to the northeast of the stellar coordinates. The 24  $\mu\text{m}$  image shows a similar 75'' arc, with higher contrast emission in the outer edges of the arc. The 24  $\mu\text{m}$  data also suggest a connection between the shocked material and the cirrus features discussed below. The 24  $\mu\text{m}$  flux density transitions from the cometary arc into the cirrus features to the east of the star more smoothly than at 8  $\mu\text{m}$ . Both the 8 and 24  $\mu\text{m}$  images show a clear spatial offset between the position of HD 34078 and the peak of the infrared emission.

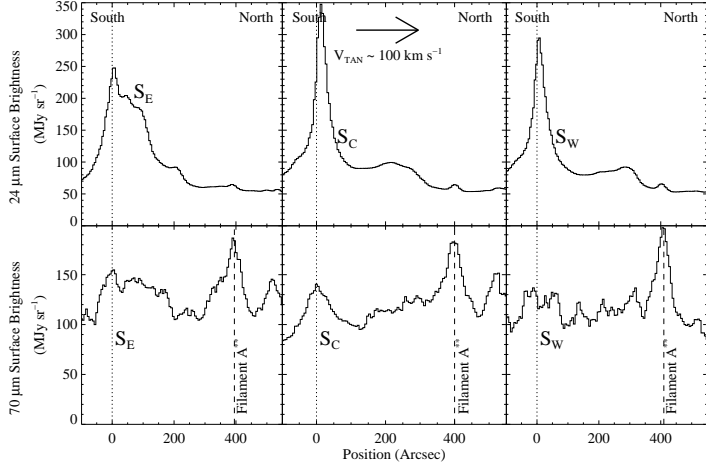


FIG. 7.— Spatial profiles of the 24 and 70  $\mu\text{m}$  MIPS scans of the southern region of IC 405. The 24  $\mu\text{m}$  data have been convolved to a resolution of  $\approx 18''$  for comparison with the 70  $\mu\text{m}$  map. The direction and magnitude of the stellar motion through IC 405 is indicated. The 24  $\mu\text{m}$  profiles outline the shock region while the 70  $\mu\text{m}$  cuts show a weaker peak near the stellar position and a maximum near the Filament A\*\* region.

TABLE 3  
24  $\mu\text{m}$  MIPS PHOTOMETRY OF NEBULAR FILAMENTS.

| Position | Program   | RA (2000)<br>(h m s) | $\delta$ (2000)<br>( $^{\circ}$ ' ") | Flux <sup>a</sup><br>(Jy) |
|----------|-----------|----------------------|--------------------------------------|---------------------------|
| A        | r16032768 | 05 16 30.99          | +34 25 03                            | $1.045 \pm 0.126$         |
| A*       | r16032768 | 05 16 19.70          | +34 25 18                            | $0.984 \pm 0.123$         |
| A**      | r16032768 | 05 16 15.52          | +34 23 58                            | $1.175 \pm 0.134$         |
| B        | r16032768 | 05 16 18.17          | +34 32 27                            | $0.892 \pm 0.117$         |

<sup>a</sup>IRS Long-Low spectra were analyzed to assess the emission line contribution to the 24  $\mu\text{m}$  band flux. Discrete lines were found to contribute less than 8% of emission in the 21.5 – 26.2  $\mu\text{m}$  bandpass.

The 4.5  $\mu\text{m}$  IRAC image is dominated by the saturated core of HD 34078 (Figure 6), but asymmetries in the PSF suggest that an enhancement exists in the direction of stellar motion. An arc is detected in the 70  $\mu\text{m}$  MIPS observations, which can be seen faintly in Figure 3.

We measured the variation in dust profile across the interaction region by taking spatial cuts through the 24 and 70  $\mu\text{m}$  MIPS data, intersecting the  $S_E$ ,  $S_C$ , and  $S_W$  positions. In order to make a fair comparison, the 24  $\mu\text{m}$  data were convolved to a resolution of  $18''$  and rebinned to the dimensions of the 70  $\mu\text{m}$  scan. The images were then aligned with a  $\sim 3^{\circ}$  rotation to account for spacecraft roll orientation and registered with their WCS data using a combination of image analysis tools (custom IDL codes as well as ds9 from the Chandra X-Ray Center and the SSC data retrieval program Leopard). We found that the registration was accurate to roughly  $2''$  in  $x$  ( $\sim$  RA) and  $10''$  in  $y$  ( $\sim$  Dec). These profiles are shown in Figure 7 running from south to north (left to right on the figure), intersecting the  $S_E$ ,  $S_C$ , and  $S_W$  coordinates listed in Ta-

ble 1.  $S_E$ ,  $S_C$ , and  $S_W$  are labeled in Figures 4 and 5, with dashed lines representing the cuts in Figure 5. The 24  $\mu\text{m}$  profiles show the dominance of the bow shock, again noting that the peak brightness regions (10 – 25'' from HD 34078) are likely saturated. The position of HD 34078 is indicated with the dotted line at 0 and the direction of stellar motion through the nebula is labeled in the center panel. The  $S_E$  profile shows the largest breadth due to its association with the cirrus-like structures. The 70  $\mu\text{m}$  profiles show an enhancement in the shocked region, but rise to a maximum at the intersection of the nebular arm containing Filament A\*\* ( $y \approx 400''$ , marked with the dashed line in Figure 7). The second peak in the 70  $\mu\text{m}$   $S_E$  and  $S_C$  profiles near 520'' are associated with the intersection of Filament A\*. We also observe an additional peak at the intersection of the Filament B arm, but we do not show a comparison as the image registration was of poorer quality.

Flux ratio ( $F_{24}/F_{70}$ ) profiles were made using these extractions. These profiles were interpolated onto a common spatial grid ( $\approx 4.7''/\text{pixel}$ ) before comparison. The registration in  $y$  was the primary source of uncertainty for these comparisons. These ratios were used to derive the dust temperature profile in the shocked region, discussed in §4.1.1. Photometry of the  $S_E$ ,  $S_C$ , and  $S_W$  regions was performed on the 8, 24, and 70  $\mu\text{m}$  images following the procedure described below. The photometric values for the shock regions are listed in Table 1.

*The HD 34078 Region* – The largest difference between the 8.0  $\mu\text{m}$  and optical images of IC 405 are the cirrus-like sheets of emission that are seen to the northeast of HD 34078 ( $\Delta x = -250 - 0''$ ,  $\Delta y = 0 - 300''$  in Figures 1, 4, 5, and 6). This cirrus structure extends along filaments roughly from HD 34078 into the region containing Filament A\*\*. It may be possible to observe this substructure in the optical with high spatial resolution and a narrow field of view, imaging the nebula without strong contamination from the central star (i.e. - *HST-ACS*).

These cirrus sheets are the strongest features in the 4.5  $\mu\text{m}$  IRAC images of this region (Figure 6). The region of patchy emission ( $-330'', -75''$ ) seen at 8.0  $\mu\text{m}$  is observed with a lower relative strength at 4.5  $\mu\text{m}$ . MIPS 24  $\mu\text{m}$  imaging of this region finds similar relative intensities as those seen at 4.5  $\mu\text{m}$ , strong cirrus sheets to the northeast of the star, with much lower relative intensity features coincident with the patchy 8.0  $\mu\text{m}$  and “shell” structure. This suggests that there is a common dust component responsible for the cirrus emission seen at 4.5, 8.0, and 24  $\mu\text{m}$ , while there is an additional component contributing to the 8.0  $\mu\text{m}$  flux in the “shell” region. This additional 8.0  $\mu\text{m}$  component is most likely a combination of an increased contribution from the 7.7 and 8.6  $\mu\text{m}$  AEFs. One of the results of the IRS scans of the bright filaments, discussed below, is that the percentage contribution of AEFs to the total flux in a given imaging band increases in the brightest knots. We propose that the regions showing an enhanced brightness in the 8.0  $\mu\text{m}$  IRAC band relative to the dust emission at 4.5 and 24  $\mu\text{m}$  are favorable for survival of the AEF carriers.

*Filament A* - Filaments A\* and A\*\* were covered by all four IRAC imaging fields and the MIPS scans at both 24 and 70  $\mu\text{m}$ . A portion of Filament A was lost at the edge of the 70  $\mu\text{m}$  map, but covered in all other bands

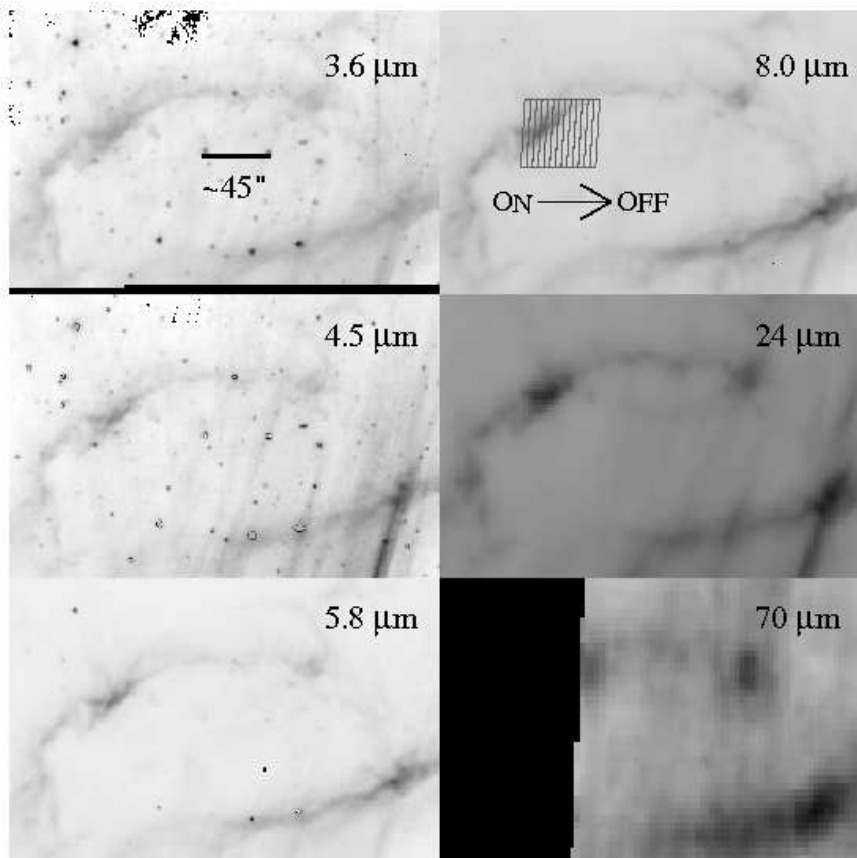


FIG. 8.— Six-color imaging of the Filament A, A\*, and A\*\* regions. Data from the four IRAC bands and two MIPS bands are shown at their original resolution, with intensity scales intended to display the nebular structure. The black regions on the 3.6 and 70  $\mu\text{m}$  images were not observed. The overlays shown on the 8.0  $\mu\text{m}$  image represent the IRS-SL aperture scan direction and the ON/OFF convention used in this work. This spectroscopy indicates that the AEFs make an important contribution to the nebular emission at positions of peak filament brightness.

(Figure 8). The 3.6  $\mu\text{m}$  images of this region display a peak along the star-facing edge of the clouds containing the filaments. The filaments are seen at 4.5  $\mu\text{m}$ , though faint compared to the cirrus features seen near the star at this wavelength. The 4.5  $\mu\text{m}$  images were the weakest (in units of  $\text{MJy sr}^{-1}$ ) in our filamentary imaging. We found the 4.5, 5.8, and 8.0  $\mu\text{m}$  bands to be tracing the same spatial regions, with the 5.8 and 8.0 bands enhanced relative to the 4.5  $\mu\text{m}$ . Again, this is attributed to additional flux from AEFs in the 5.8 and 8.0  $\mu\text{m}$  bands.

The 24 and 70  $\mu\text{m}$  MIPS images of Filament A show consistency with the 8.0  $\mu\text{m}$  reference image. The 24  $\mu\text{m}$  map shows an additional flare structure pointing from Filament A\*\* to the northwest (RA =  $05^{\text{h}}16^{\text{m}}14.49^{\text{s}}$ ,  $\delta = +34^{\circ}24'47.0''$ , J2000). This feature is also seen weakly at 4.5  $\mu\text{m}$ .

Nebular photometry (at 8, 24, and 70  $\mu\text{m}$ ) of Filaments A and B was performed and the flux densities are presented in Tables 2, 3, and 4. To ensure a fair comparison, the spatial resolution of the 8.0  $\mu\text{m}$  IRAC image and the 24  $\mu\text{m}$  MIPS scan were degraded. A two-dimensional Gaussian kernel was convolved with the data to produce

8 and 24  $\mu\text{m}$  images with an effective resolution of about  $18''$ , comparable to that of the 70  $\mu\text{m}$  map (Rieke et al. 2004). The convolved images were integrated over a discrete number of pixels and multiplied by the solid angle subtended by each pixel,  $3.4 \times 10^{-11} \text{ sr pixel}^{-1}$  at 8  $\mu\text{m}$ ,  $1.5 \times 10^{-10} \text{ sr pixel}^{-1}$  at 24  $\mu\text{m}$ , and  $5.8 \times 10^{-10} \text{ sr pixel}^{-1}$  at 70  $\mu\text{m}$ .

We chose the photometric extraction regions based on the sizes of the filaments in the 8.0  $\mu\text{m}$  data. We found that the central cores of all four filament positions could be contained in a box of roughly  $20'' \times 20''$ . A 20 pixel square used at 8  $\mu\text{m}$ , a 10 pixel square was used in the 24  $\mu\text{m}$  band, and a 5 pixel square extraction was used for the 70  $\mu\text{m}$  MIPS data. These extraction regions are of the same order as the projected size of the *FUSE* LWRS aperture ( $30'' \times 30''$ ) used at Filaments A and B (Figure 1). The photometric measurements were used to constrain the nebular dust temperature in IC 405, as discussed in §4.1 and §4.2.

*Filament B* - The Filament B region is located  $\approx 1000''$  north of HD 34078, a part of what Herbig (1958) labels the “E nebulosity”. This is a position

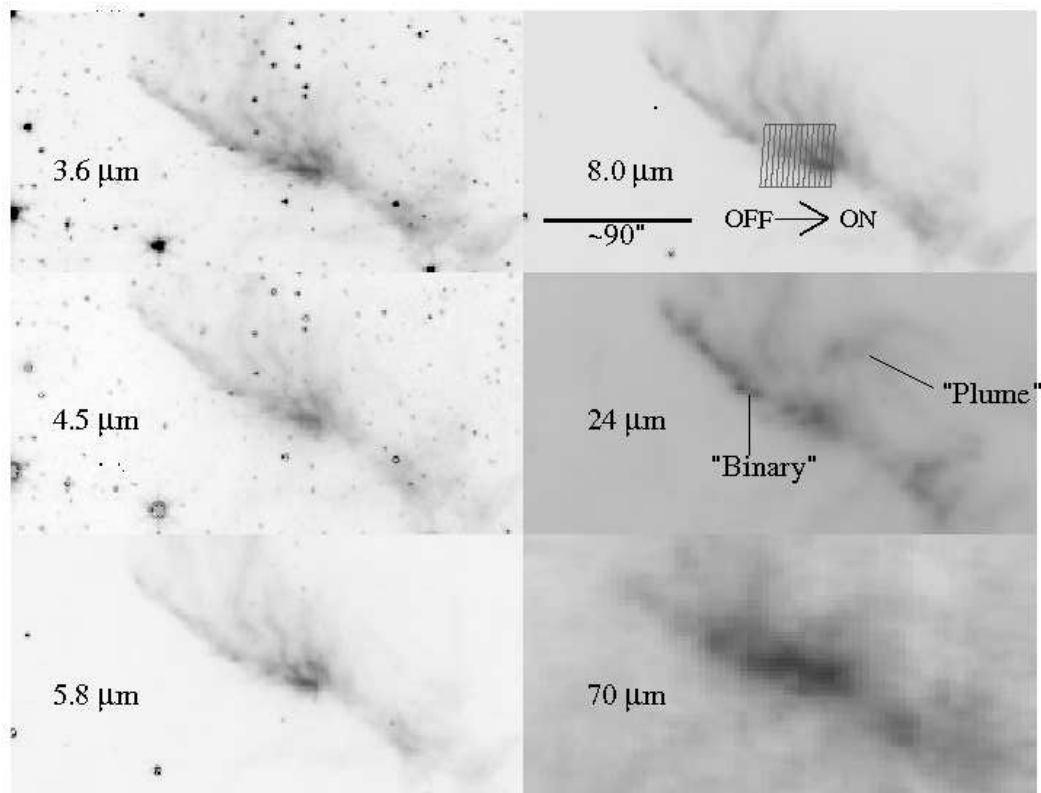


FIG. 9.— Six-color imaging of the Filament B region. Data from the four IRAC bands and two MIPS bands are shown at their original resolution. The images are qualitatively similar, but quantitative analysis shows that the South (HD 34078-facing) edge of filament is more extended at  $24\ \mu\text{m}$ , suggesting that the carriers of the AEFs are being destroyed in the tenuous interfilament medium. The  $24\ \mu\text{m}$  map also shows a “Plume” to the north and a “Binary” feature to the northeast of the main Filament B emission, not seen as distinctly in other bands. Again, the overlays shown on the  $8.0\ \mu\text{m}$  image represent the IRS-SL aperture scan direction and the ON/OFF convention.

TABLE 4  
70  $\mu\text{m}$  MIPS PHOTOMETRY OF NEBULAR FILAMENTS.

| Position | Program                | RA (2000)<br>( <sup>h</sup> <sup>m</sup> <sup>s</sup> ) | $\delta$ (2000)<br>( <sup>°</sup> <sup>'</sup> <sup>''</sup> ) | Flux<br>(Jy)      |
|----------|------------------------|---|--|-------------------|
| A        | partially off scan map | —   | —  | —                 |
| A*       | r16032768              | 05 16 19.66   | +34 25 20  | $2.562 \pm 0.193$ |
| A**      | r16032768              | 05 16 15.64   | +34 23 50  | $3.141 \pm 0.214$ |
| B        | r16032768              | 05 16 17.74   | +34 32 32  | $2.356 \pm 0.186$ |

where *FUSE* detected fluorescent emission from  $\text{H}_2$  as the most prominent spectral feature from  $\text{Ly}\beta$  to  $1190\ \text{\AA}$  (France et al. 2004). Filament B was covered in all six imaging bands used in this work as well as with spectroscopic scans. Unlike the southern filaments described above, all four IRAC bands appear to be tracing the same material in the Filament B region. They show the same northeast-to-southwest elongated filamentary structure with a peanut-shaped central concentration. This peanut-shaped central structure, shown in all six IR imaging bands in Figure 9, is the center of Filament B (RA =  $05^{\text{h}}16^{\text{m}}16.88^{\text{s}}$ ,  $\delta = +34^{\circ}32'21.0''$ , J2000).

The MIPS scans at  $24$  and  $70\ \mu\text{m}$  follow the structure seen in the IRAC bands, with a few noteworthy exceptions. The MIPS data show that the southern edge of the region occurs closer to the star at  $24\ \mu\text{m}$  than at the IRAC wavelengths. The  $24\ \mu\text{m}$  brightness increases gradually ( $B_{24} 47 - 61\ \text{MJy sr}^{-1}$ ) over a  $\sim 30''$  transition region onto Filament B, while the  $8.0\ \mu\text{m}$  brightness rises more abruptly at the edge of the filament, increasing in brightness by more than a factor of two ( $B_8 18 - 40\ \text{MJy sr}^{-1}$ ) over a  $15''$  interface region. Destruction of small grains and the carrier of the  $7.7\ \mu\text{m}$  AEF in the more tenuous environment south of Filament B could produce

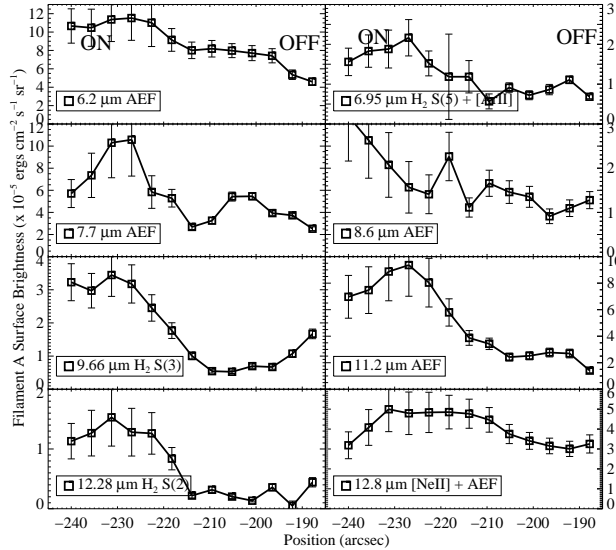


FIG. 10.— Filament A line strengths measured with the Short-Low module on the IRS, as a function of position. The coordinates correspond to the  $8.0 \mu\text{m}$  reference image, Figure 1. The map goes from East ( $-245''$ , on the core of the filament) to West ( $> -220''$ , off of the peak of the  $8.0 \mu\text{m}$  filament emission).

this effect. We may be seeing the erosion of this cloud in progress, the strong UV field of HD 34078 photoevaporating the carbonaceous grains and weakly shielded molecules. This idea could be tested by searching for the remnants of these species ( $[\text{C II}] \lambda 158 \mu\text{m}$  for example; van Dishoeck 2004) with future far-IR spectroscopic instrumentation, such as *Herschel*-PACS (Poglitsch et al. 2004).

The  $24 \mu\text{m}$  MIPS data also reveal a plume of material to the north-northwest of the main knot of Filament B (RA =  $05^{\text{h}}16^{\text{m}}16.74^{\text{s}}$ ,  $\delta = +34^{\circ}33'09.5''$ , J2000). The IRAC images show hints of emission at this location, but only at  $24 \mu\text{m}$  is the contrast high enough to identify this plume as a separate feature. It is worth noting that this plume seems to be “in the shadow” of Filament B, analogous to the position of the flare filament seen in the shadow of Filament A\*\* at  $24 \mu\text{m}$ . The other notable feature seen in the MIPS imaging is the binary structure seen to the northeast of Filament B at  $24 \mu\text{m}$  (RA =  $05^{\text{h}}16^{\text{m}}21.75^{\text{s}}$ ,  $\delta = +34^{\circ}32'41.9''$ , J2000). The two components of this feature are not spatially resolved at  $70 \mu\text{m}$ . The “Plume” and “Binary” features are labeled on Figure 8.

Integrated flux densities for Filament B were measured from the IRAC 8.0, MIPS 24, and MIPS  $70 \mu\text{m}$  images. The values are listed in Tables 2, 3, and 4. We find the  $24/70 \mu\text{m}$  ratio to be essentially identical in Filaments A\*, A\*\*, and B ( $0.379 \pm 0.005$ ), indicative of similar dust temperatures in the three regions (§4.2).

### 3.2. Spectroscopy: IRS

*Filament A* - The IRS scan maps of Filament A have been used to measure the variations in emission characteristics from dense knots to tenuous nebular material. The spatial and spectral coverage of the Short-Low ( $5 - 15 \mu\text{m}$ ) module is best suited to studying the change in

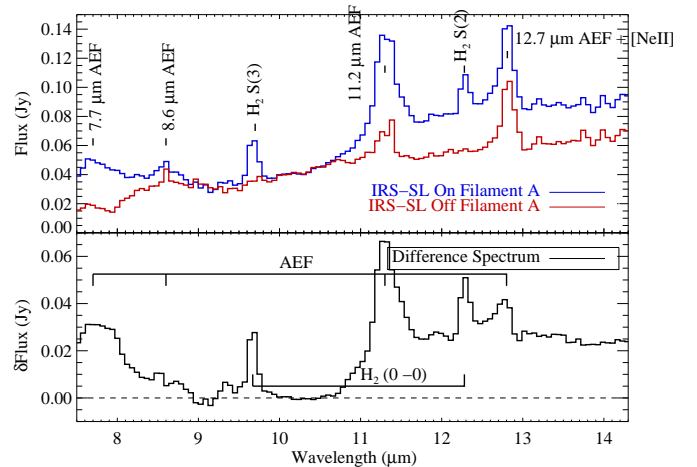


FIG. 11.— IRS spectra of the ON-filament and OFF-filament regions near Filament A. The OFF-Filament was scaled up to the ON-filament flux level in the  $10 \mu\text{m}$  region. The ON-filament (top panel, blue) spectrum shows the  $7.7$  and  $11.2$  AEFs,  $\text{H}_2$ , and the  $11 - 14 \mu\text{m}$  “plateau” to be enhanced compared to the OFF-filament (top panel, red) pointing. The bottom panel shows the difference of the ON and OFF-filament spectra to illustrate the differences.

AEF signature while scanning across the region of interest in full-slitwidth steps. Filament A was mapped from east to west, with the eastern portion of the map being located on the brightest parts of Filament A, while the western portion was off the brightest Filament A emission (Figure 10).

All observed emission lines follow the same generic trend: They are brightest near the peak of the  $8.0 \mu\text{m}$  reference image, and their intensity falls off with distance from the peak (Figure 10). The AEFs at  $6.2$ ,  $8.6$ , and  $11.2$  were detected clearly at all Filament A pointings. Band substructure in the  $6.2 \mu\text{m}$  feature is discussed in §4.4. Line strengths were measured by integrating the spectra over the wavelengths of interest (in the case of the  $7.7 \mu\text{m}$  band, the  $1^{\text{st}}$  and  $2^{\text{nd}}$  orders were joined before measurement). The continuum contribution was removed by subtracting a linear fit to the continuum over the wavelengths spanned by the line. The  $7.7 \mu\text{m}$  AEF was seen to be the most variable spectral feature, ranging from marginally detectable off the filament to a wide ( $\Delta\lambda \sim 1 \mu\text{m}$ ) band at the peak of the filament brightness. For all IRS-SL spectral lines, we conservatively assumed a 20% flux error on each measurement (line and continuum) which resulted to total line strength uncertainties of a few to approximately 30%.

Figure 11 shows examples of the low-dispersion spectra acquired at Filament A, showing several aromatic and  $\text{H}_2$  emission lines. The spectra obtained on the peak of the  $8 \mu\text{m}$  emission also show a broad “plateau” feature from  $11 - 14 \mu\text{m}$  that is not seen in the spectra obtained off the filament. This plateau was first seen by *IRAS* (Cohen et al. 1985), and *Spitzer* detected a similar  $10.5 - 14.5 \mu\text{m}$  feature in NGC 7023, however in that nebula the individual features wash out into a broad  $\Delta\lambda \approx 2 \mu\text{m}$  feature farther from the central star (Werner et al. 2004b). A similar effect with distance

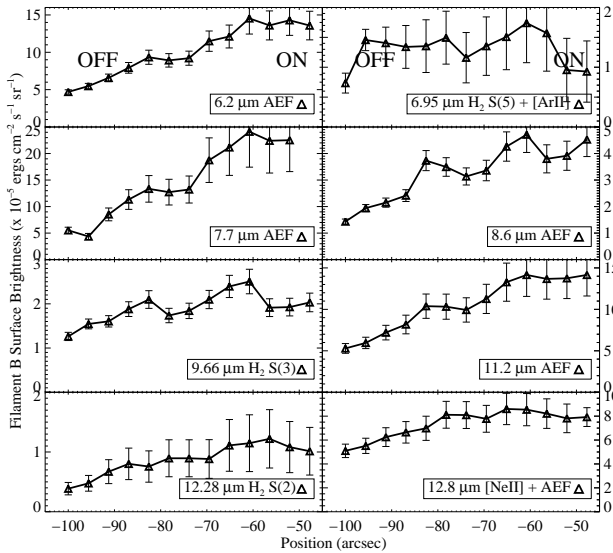


FIG. 12.— Filament B line strengths measured with the Short-Low module on the IRS, as a function of position. The coordinates correspond to the  $8.0 \mu\text{m}$  reference image, Figure 1. The map goes from East ( $-105''$ , off of the filament) to West ( $> -70''$ , near the peak of the  $8.0 \mu\text{m}$  filament emission).

from the illuminating star was seen by Cesarsky et al. (2000) in the reflection nebula Ced 201. In the case of IC 405 however, the entire spectroscopic scan of Filament A is roughly equidistant from HD 34078, thus we are most likely not observing an evolution with radiation field. The imaging indicates that the spectra sample less dense regions as the scan moves off the filament. This result would be consistent with the  $11 - 14 \mu\text{m}$  plateau being controlled by density<sup>4</sup>.

Mid-IR spectra of the Orion Bar (Bregman et al. 1989) indicate that the molecules responsible for the  $11 - 13 \mu\text{m}$  plateau are independent of the carriers of the narrower AEFs. In IC 405, the AEFs, as well as the lines of  $\text{H}_2$  and  $12.8 \mu\text{m}$  AEF+[Ne II] (described below), show an increase in peak flux with the plateau strength. Figure 11 illustrates the changes in these features. The top panel shows a comparison between spectra observed at the peak of the filament brightness and spectra observed off the filament. The “off” spectrum is scaled to the  $10.0 - 10.5 \mu\text{m}$  region of the “on” spectrum. The difference of the two is plotted in the lower panel. The relative strengths of the  $7.7 \mu\text{m}$  feature, the  $\text{H}_2$  lines, and the  $11.2$  and  $12.8 \mu\text{m}$  features are all enhanced with the  $11 - 14 \mu\text{m}$  plateau.

Several atomic emission lines produced in ionized gas were observed in the Short-High observations clustered on the brightest region of Filament A, but we only report on the species that appear in more than 15 of the 25 pointings. These spectra show strong [Ne II]  $\lambda 12.81 \mu\text{m}$  at all positions. In the low dispersion spectra of Filament A, the average central wavelength of the  $12.8 \mu\text{m}$  feature is observed at  $\langle \lambda_{obs} \rangle = 12.817 \pm 0.005 \mu\text{m}$ , con-

sistent with the observed emission coming from ionized neon as opposed to the  $12.7 \mu\text{m}$  AEF. In addition to [Ne II], [S III]  $\lambda 18.71 \mu\text{m}$  is detected in most of the high dispersion data. We note that it is interesting to find these energetic ions (ionization potentials are  $> 21 \text{ eV}$  for Ne II and S III) spatially aligned with the emission lines of  $\text{H}_2$ , described below. One might naively expect that the molecules would be destroyed in a region with highly excited ions, yet they are observed within the same  $4.7'' \times 11.3''$  (IRS Short-High aperture) region. This may suggest that the  $\text{H}_2$  in IC 405 resides in dense globular reservoirs, as in planetary nebulae (Huggins et al. 2002; Speck et al. 2003; Lupu et al. 2006; Hora et al. 2006). Narrow band near-IR imaging in the rovibrational emission lines of  $\text{H}_2$  ( $\lambda \sim 2 \mu\text{m}$ ) would be useful in testing this suggestion. Finally, we detect emission lines at  $12.94$  and  $13.14 \mu\text{m}$  in the majority of the Short-High spectra at a signal to noise ratio comparable to the  $\text{H}_2$  lines discussed below. The  $12.94 \mu\text{m}$  line remains unidentified, but we tentatively identify the  $13.14 \mu\text{m}$  feature as the O I  $\lambda\lambda 13.139 - 13.157 \mu\text{m}$  multiplet. Hot pixels in the Short-High module do not appear to be the source of the unidentified lines, however, the  $13.14 \mu\text{m}$  line does appear as a single pixel in some of the pointings. Given the possibility of hot pixel contamination and the fact that the excitation process for the neutral oxygen line is unclear, we do not feel that this is a conclusive detection.

The pure rotational emission lines of  $\text{H}_2$  are seen at the on-filament pointings. The  $(0 - 0)$  S(5), S(3), and S(2) lines are strongest in the core of Filament A, becoming weaker in all directions outside of the brightest  $20''$ . The S(4) line was only weakly observed in one pointing. The S(5) line of  $\text{H}_2$  is likely blended with [Ar II], as we measure a line center that lies between the rest wavelengths for the molecular and atomic lines,  $\lambda_{obs} = 6.946 \pm 0.010$ , where as  $\lambda_{S(5)} = 6.91$  and  $\lambda_{[Ar II]} = 6.99 \mu\text{m}$ . The continuum subtraction for the S(3) and S(2) lines is somewhat uncertain due to the variability of the AEFs on whose wings they reside. Due to concerns about what effects this may have on the determination of the  $\text{H}_2$  rotational temperature ( $T(\text{H}_2)$ ), we also used observations of the brightest filamentary regions with the Short-High IRS module to make clean measurements of the  $\text{H}_2$   $(0 - 0)$  S(2)  $\lambda 12.28$  and S(1)  $\lambda 17.03 \mu\text{m}$  lines when they are seen at high S/N. The determination of  $T(\text{H}_2)$  is discussed in §4.2.

The contributions from the  $6.2$ ,  $7.7$ , and  $8.6 \mu\text{m}$  AEFs to the  $5.8$  and  $8.0 \mu\text{m}$  IRAC bands were measured in Filament A. Line strengths were determined as described above, and compared to the total spectroscopic flux measured in the IRS data over the  $5.8$  and  $8.0 \mu\text{m}$  IRAC imaging windows (Fazio et al. 2004; Werner et al. 2004a). We found that the  $6.2 \mu\text{m}$  feature was responsible for  $\sim 33 - 57\%$  of the emission in the  $5.8 \mu\text{m}$  IRAC band, with a peak in the AEF contribution coincident with the peak in  $5.8 \mu\text{m}$  brightness. The relative contributions from  $\text{H}_2$  S(5)+[Ar II] ( $\lambda \approx 6.95 \mu\text{m}$ ), and the  $7.7$  and  $8.6 \mu\text{m}$  AEFs were measured in the IRAC  $8.0 \mu\text{m}$  bandpass. The  $\text{H}_2$  S(5)+[Ar II] was negligible off the filament and rose to a maximum of  $3\%$  at the peak  $8.0 \mu\text{m}$  brightness. The  $8.6 \mu\text{m}$  AEF contributes  $1.0 - 1.5\%$  at all positions, while the  $7.7 \mu\text{m}$  AEF showed a strong increase on the filament. At the western end of the IRS

<sup>4</sup> We note that while IR flux density images are representative of the underlying density structure, the IRAC flux density does not strictly reflect the nebular density (Heitsch et al. 2006).

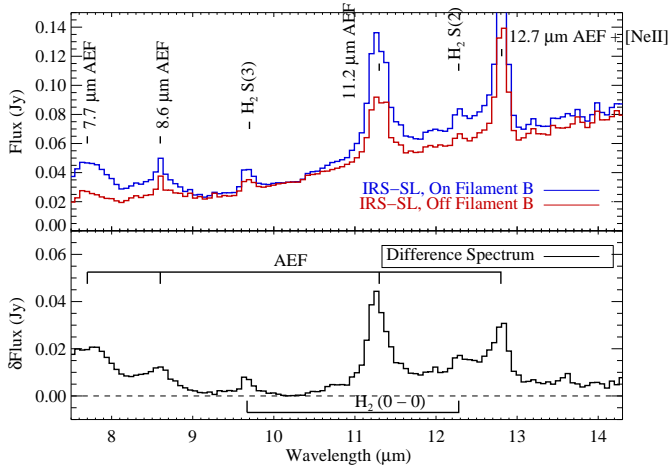


FIG. 13.— IRS spectra of Filament B. The blue spectrum in the top panel was acquired on the peak of the  $8.0 \mu\text{m}$  emission, while the red spectrum was acquired off of the brightest region of the filament. The OFF-filament spectrum was scaled to the ON-filament flux between  $10 - 10.5 \mu\text{m}$ . The difference of the two spectra is plotted in the lower panel. The strengths of the pure rotational  $\text{H}_2$  lines and the  $11 - 14 \mu\text{m}$  plateau are observed to be less variable than at Filament A (Figure 11).

scan (the "OFF" filament position) the  $7.7 \mu\text{m}$  feature contributes about 8% of the flux in the  $8.0 \mu\text{m}$  image, increasing to 34% at the peak of the  $8.0 \mu\text{m}$  brightness. Following this argument and noting the brightness of the  $3.6 \mu\text{m}$  images relative to  $4.5 \mu\text{m}$ , we consider it likely that a substantial fraction of the  $3.6 \mu\text{m}$  brightness is due to emission from the  $3.3 \mu\text{m}$  AEF, although we note that the scattered starlight component increases at shorter wavelengths as well.

*Filament B* - The dust,  $\text{H}_2$ , and atomic lines observed in the Short-Low spectra of Filament B follow two behaviors. The  $6.2$ ,  $7.7$ ,  $8.6$ , and  $11.2 \mu\text{m}$  AEFs show a roughly linear increase in brightness as the scan moves onto the filament, while  $\text{H}_2 \text{ S}(5)+[\text{Ar II}]$ ,  $\text{H}_2 \text{ S}(3)$  and  $\text{S}(2)$ , and  $\text{AEF}+[\text{Ne II}] \lambda 12.8 \mu\text{m}$  show a rise in strength then flatten out across the filament. This is shown in Figure 12. Examples of the spectra obtained at Filament B are shown in Figure 13. The  $11 - 14 \mu\text{m}$  plateau is also observed at the filament position, although with less variability than at Filament A. The Short-High spectra were again used to cleanly measure the  $\text{S}(2)$  and  $\text{S}(1)$  lines near the peak of the Filament B brightness. As in Filament A, we detect  $[\text{Ne II}] \lambda 12.81$  and  $[\text{S III}] \lambda 18.71 \mu\text{m}$  at the majority of the pointings. The  $\lambda 12.94$  and  $\lambda 13.14 \mu\text{m}$  features are observed as well.

Following the procedure outlined for Filament A, we measured the contribution of line emission to the  $5.8$  and  $8.0 \mu\text{m}$  images. The  $6.2 \mu\text{m}$  AEF is an appreciable fraction of the  $5.8 \mu\text{m}$  IRAC band brightness, ranging from 40% at the eastern end of the scan map (OFF filament) to 46% at the peak of the Filament B. The  $\text{H}_2 \text{ S}(5)+[\text{Ar II}]$  blend makes up 2.8% of the nebular flux off the filament, dropping to 1.5% on the center of the filament. This is opposite the behavior seen at Filament A, where the relative  $\text{H}_2+[\text{Ar II}]$  contribution increased with filament brightness. The  $7.7$  and  $8.6 \mu\text{m}$  AEFs relative contri-

bution to the  $8.0 \mu\text{m}$  image increases substantially with position. Both lines contribute roughly 2.5 times more to the ON filament positions than they do in the more diffuse nebular pointings. The  $7.7 \mu\text{m}$  AEF rises from 13 to 35% while the  $8.6 \mu\text{m}$  feature increases from 2 to 5%.

### 3.3. Regional Comparison

We can compare the general characteristics of Filament B to those of Filament A (Table 5). The  $\text{H}_2$  rotational emission lines are brighter in Filament A, which could indicate a higher  $\text{H}_2$  density in Filament A or possibly a higher photoelectric grain heating rate due to the relative proximity of HD 34078 (Hollenbach & Tielens 1997; Abel et al. 2005). Similarly, we observe  $24 \mu\text{m}$  emission, presumably emission from grains, to be brighter in Filament A. Again, we would expect the grain population nearer the illuminating star to display an enhanced brightness. However, the AEFs show the opposite behavior, they are seen to be anti-correlated with the strength of the far-UV radiation field. The  $6.2$ ,  $7.7$ ,  $8.6$ , and  $11.2 \mu\text{m}$  AEFs all have a position averaged brightness higher in Filament B. The  $8.0 \mu\text{m}$  photometric measurements are higher in Filament B, consistent with a considerable contribution from a brighter  $7.7 \mu\text{m}$  feature. As the AEF carriers and small ( $a \lesssim 30 \text{ \AA}$ ) grains are thought to be heated stochastically by the absorption of a single UV photon (Draine & Li 2001), one might expect the AEF flux to be higher near HD 34078. We suggest that the opposite behavior may be caused by increased photodestruction of the AEF carriers in the more intense UV radiation field at Filament A. The large column density of hydrogen, relative to the aromatics, may place the  $\text{H}_2$  in a self-shielding regime while the AEF carriers are more easily dissociated by the UV radiation field of HD 34078. An analogous situation is seen in UV illuminated PDRs where  $\text{H}_2$  is observed while the lower column density, unshielded, CO is destroyed (Luhman & Jaffe 1996; Luhman et al. 1997).

IRS mapping observations of the shock region were not part of the P20434 program, but predictions about the spectral characteristics of the region can be made.  $\text{H}_2 (0-0) \text{ S}(3) \lambda 9.66 \mu\text{m}$ ,  $(1-0) \text{ S}(1) \lambda 2.12 \mu\text{m}$ , and  $[\text{O I}] \lambda 63 \mu\text{m}$  should be readily observable in this region (van Buren et al. 1990). Draine et al. (1983) make predictions about cooling through additional rotational lines of  $\text{H}_2$ , as well as CO, OH,  $\text{H}_2\text{O}$ , and  $[\text{C I}]$ .

## 4. DISCUSSION

### 4.1. Cometary Bow Shock Associated with HD 34078

Far-IR bow shocks are found around roughly 30% of galactic O and B runaway stars (van Buren et al. 1995; Noriega-Crespo et al. 1997). These stars are ejected from their formation site by interactions, primarily with either a supernova binary companion or members of the cluster in which they were formed (Huthoff & Kaper 2002). When one of these high space velocity ( $\geq 30 \text{ km s}^{-1}$ ) stars encounters even moderately dense interstellar material, a bow shock is formed by ram pressure confinement of the OB stellar wind as it moves through the ambient medium (van Buren & McCray 1988; Noriega-Crespo et al. 1997). UV radiation from the star heats the shocked gas and dust, producing excess far-IR emission in these shock regions, which has been observed by *IRAS*.

TABLE 5  
FILAMENT A AND B MOLECULAR LINE STRENGTH AND DUST BRIGHTNESSES.

|                | <i>Spitzer</i><br><i>FUSE</i>   | Filament A<br>Pos3  | Filament B<br>Pos4   |
|----------------|---|---|--|
| Species        |   |   |  |
| H <sub>2</sub> | $\langle\langle(0-0) S(3) \text{ Brightness}\rangle\rangle^a$<br>$\langle\langle(0-0) S(2) \text{ Brightness}\rangle\rangle$<br>UV Brightness <sup>b</sup><br>T(H <sub>2</sub> ) (K) <sup>c</sup> | $2.84 \pm 0.62$<br>$1.22 \pm 0.23$<br>$2.00 \pm 0.60$<br>$418^{+108}_{-73}$ | $2.14 \pm 0.25$<br>$1.08 \pm 0.12$<br>$0.40 \pm 0.16$<br>$387^{+46}_{-39}$ |
| AEFs           | $\langle 6.2 \mu\text{m Brightness}\rangle$<br>$\langle 7.7 \mu\text{m Brightness}\rangle$<br>$\langle 8.6 \mu\text{m Brightness}\rangle$<br>$\langle 11.2 \mu\text{m Brightness}\rangle$         | $8.73 \pm 2.23$<br>$8.52 \pm 2.31$<br>$1.69 \pm 0.66$<br>$5.05 \pm 2.79$    | $10.13 \pm 3.39$<br>$9.39 \pm 3.89$<br>$3.30 \pm 1.03$<br>$10.58 \pm 3.16$ |
| Blends         | $\langle \text{H}_2 + [\text{Ar II}] 6.95 \mu\text{m Brightness}\rangle$<br>$\langle \text{AEF} + [\text{Ne II}] 12.8 \mu\text{m Brightness}\rangle$  | $1.23 \pm 0.50$<br>$4.04 \pm 0.77$  | $1.29 \pm 0.28$<br>$7.35 \pm 1.15$   |
| Dust           | F <sub>24</sub> (Jy)<br>F <sub>70</sub> (Jy)  | $1.045 \pm 0.126$<br>-  | $0.892 \pm 0.117$<br>$2.356 \pm 0.186$                                     |

<sup>a</sup>H<sub>2</sub> brightnesses are averages over six ON filament pointings at each position. AEF and Blend brightnesses are averages over all IRS-SL pointings at each filament. They are in units of ( $\times 10^{-5}$  ergs cm<sup>-2</sup> s<sup>-1</sup> sr<sup>-1</sup>).

<sup>b</sup>Measured over the  $\sim 1100$  Å line complex (1097.7 – 1108.0 Å).

<sup>c</sup>Measured from the  $(I(S(3))/I(S(2)))$  ratio. Filament A shows evidence for temperature fluctuations to T(H<sub>2</sub>)  $\sim 700$  K (see §4.2).

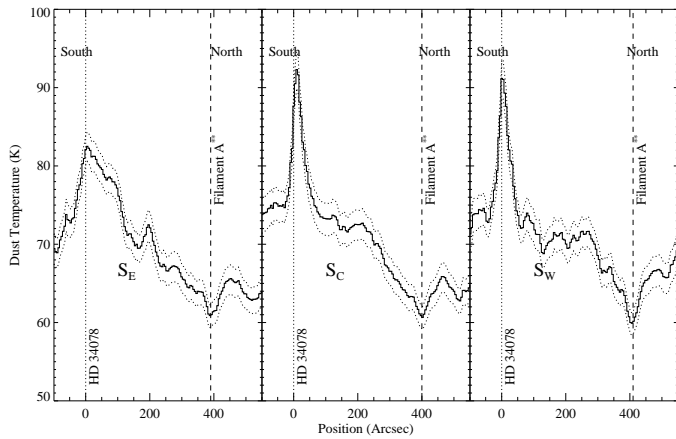


FIG. 14.— Dust temperature profiles of the southern portion of IC 405, from HD 34078 (at the origin) to Filament A\*\*. The error ranges are plotted as dotted lines. The temperature profiles are created by taking the ratio of spatial extractions from the 24 and 70  $\mu\text{m}$  MIPS scans. The dust temperature is seen to rise sharply at the location of the bow shock, 10 – 25'' north of HD 34078. The minimum dust temperature of  $\sim 60$  K is observed at the position of Filament A\*\*. This temperature is characteristic of the dense filaments in IC 405.

HD 34078 was a bow shock candidate in the *IRAS* survey of van Buren et al. (1995), showing an excess brightness at 60  $\mu\text{m}$ , but no shock morphology could be detected. A higher spatial resolution (1') follow up to this survey (Noriega-Crespo et al. 1997) did not resolve the shock. It is only the imaging capabilities of *Spitzer* ( $\leq 6''$  at  $\lambda \leq 24 \mu\text{m}$ ) that allow us to unambiguously identify the HD 34078 bow shock. Figures 4 and 5 show the stellar region at 8 and 24  $\mu\text{m}$ ,

identifying the three shock regions of interest, as described in §3.1. Inspection of the images makes clear the “cometary” morphology (van Buren et al. 1990), though the  $\sim 75''$  diameter arc is more extended than traditional ultracompact H II regions that are interpreted as bow shocks (Mac Low et al. 1991).

#### 4.1.1. Temperature Structure

The dust in the bow shock region should be heated by the UV radiation field of HD 34078, and we use spatial extractions of the 24 and 70  $\mu\text{m}$  MIPS maps to confirm this prediction. The F<sub>24</sub>/F<sub>70</sub> ratio cuts have been converted into dust temperature profiles as a function of position following the modified black body prescription described in §4.2. The dust temperature profiles for the S<sub>E</sub>, S<sub>C</sub>, and S<sub>W</sub> regions are shown in Figure 14. These cuts extend from roughly 100'' south of HD 34078 to 550'' north of the star, intersecting the Filament A\*\* region. We observe the  $\sim 60$  K filament temperature derived below for Filament A\*\*, and see the rise in dust temperature near HD 34078, increasing sharply in the inner 100'' to a peak that is coincident with the location of the cometary morphology on the images. The peak dust temperatures for the shock regions are  $T_{d,peak}^{S_E} = 82.5 \pm 1.9$ ,  $T_{d,peak}^{S_C} = 92.3 \pm 2.4$ , and  $T_{d,peak}^{S_W} = 91.2 \pm 2.5$ , respectively. These peak temperatures are lower limits as the 24  $\mu\text{m}$  MIPS data were saturated along a portion of the bright bow shock ridge. The dust temperatures derived from the photometric measurements (given in Table 1) of the shock region average over the peak 24  $\mu\text{m}$  brightness and the surrounding emission.

The dust temperatures we derive are factors of 2 – 3 higher than seen in the original *IRAS* bow-shock survey (van Buren & McCray 1988). The high temperature of the HD 34078 shock can be related to the high velocity

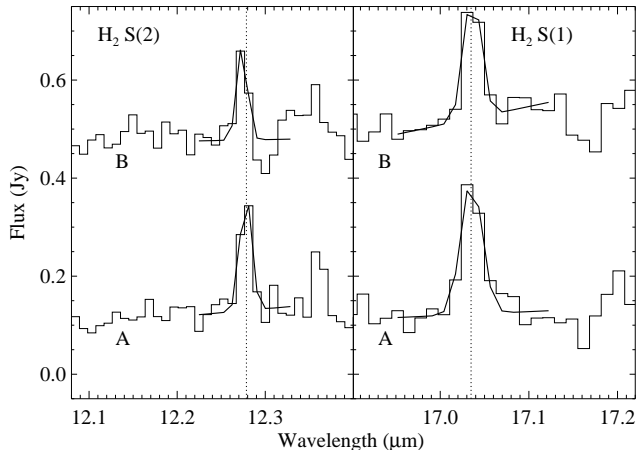


FIG. 15.— Short-High spectra of the  $\text{H}_2$  (0–0) S(2) and S(1) pure rotational emission lines at 12.28 and 17.03  $\mu\text{m}$ . An offset of 0.4 Jy was added to the Filament B spectra for this figure. Ratios of the measured line strengths ( $I(S(2))/I(S(1))$ ) are used to derive the  $\text{H}_2$  rotational temperature,  $T(\text{H}_2)$ . The  $I(S(2))/I(S(1))$  temperature in Filament B agrees with that derived from Short-Low measurement of the  $I(S(3))/I(S(2))$  temperature ( $T^B(\text{H}_2) \approx 400$  K). However, the Short-High observations of Filament A show evidence for non-uniform excitation corresponding to a temperature of roughly 700 K.

of the star and the high spatial resolution of these observations. The  $\sim 100$   $\text{km s}^{-1}$  velocity of HD 34078 is outside the range of velocities considered by van Buren et al. (1995). HD 34078 has the largest one-dimensional proper motion (within the errors) of these shock candidates ( $pm_y$  in Table 2 of van Buren et al. 1995). The high spatial resolution provided by *Spitzer*-MIPS allows us to spatially resolve the hottest shock regions. The larger *IRAS* beam (5' for van Buren et al 1995; and 1' for Noriega-Crespo et al. 1997) sampled the entire shock region, diluting the warmer inner regions with cooler dust on the exterior of the shock. Averaged over 5' around HD 34078 ( $-90 - 210''$  of Figure 14), the temperature derived for  $S_C$  decreases to 76 K.

#### 4.1.2. Bow Shock Density: $\text{H}_2$ Excitation and UV Dust Extinction

The morphological and thermal evidence places the HD 34078/IC 405 interface in the cometary bow shock family, and we can use the analytic models of van Buren & McCray (1988) and van Buren et al. (1990) to explore other topics related to the IC 405 system. An estimate of the nebular density enables us to calculate the column density and UV optical depth associated with the bow shock and explore the implications for existing studies.

The distance from the star to the shock region can be calculated from Equation (2) of (van Buren et al. 1990; see also van Buren & McCray 1988), assuming an existing knowledge of the nebular density. Alternatively, we can measure the star-shock distance directly from the IRAC and MIPS observations, and solve for the density. Let  $l$  be the measured distance from the star to the shock structure in the direction of motion,  $\approx 15''$  on the 8.0  $\mu\text{m}$  IRAC image. At the assumed distance of 450 pc, this corresponds to a separation of  $1.77 \times 10^{15}$  cm. Rewrit-

ing equation (2) of van Buren et al. (1990), the density ( $n_H = 2n_{\text{H}_2} + n_{\text{HI}} + n_{\text{HII}}$ ) in the region of IC 405 through which HD 34078 is currently moving is given by

$$n_H = (3.03 \times 10^{38}) \dot{m}_{*,-6} v_{w,8} \mu_H^{-1} v_{*,6}^{-2} l^{-2} \text{ cm}^{-3} \quad (1)$$

where  $\dot{m}_{*,-6}$  is the stellar wind mass loss rate in units of  $\times 10^{-6} M_\odot \text{ yr}^{-1}$ ,  $v_{w,8}$  is the terminal velocity of the stellar wind in units of  $\times 10^8 \text{ cm s}^{-1}$ ,  $v_{*,6}$  is the stellar velocity in units of  $\times 10^6 \text{ cm s}^{-1}$ , and  $\mu_H$  is the dimensionless mass per H-nucleus. We take  $\mu_H$  to be 1 and assume a stellar velocity of  $\sim 100 \text{ km s}^{-1}$  (Blaauw & Morgan 1954; Boissé et al. 2005). The stellar mass loss rate ( $\log(\dot{m}_*) = -9.5$ ) and terminal wind velocity (800  $\text{km s}^{-1}$ ) are taken from Martins et al. (2005). Following this procedure, we calculate a nebular density of  $n_H = 244 \text{ cm}^{-3}$ .

Rewriting Equation (7) of van Buren et al. (1990), the column density of the swept-up material is given by

$$N = (1.95 \times 10^{19}) \dot{m}_{*,-6}^{1/2} v_{w,8}^{1/2} \mu_H^{-1/2} v_{*,6}^{-1} n_H^{1/2} \text{ cm}^{-2} \quad (2)$$

with the parameters defined as before. This calculation yields a column density of material piled-up by the intrusion of HD 34078,  $N = 4.8 \times 10^{17} \text{ cm}^{-2}$ . This value is very similar to the  $\text{H}_2$  column density found by Boissé et al. (2005) for the hot absorption component along the HD 34078 line of sight. They find  $N(\text{H}_2, J \geq 5) = 3.3 \times 10^{17} \text{ cm}^{-2}$ , comparable to their model prediction of  $2.4 \times 10^{17} \text{ cm}^{-2}$ . Our derived column density of the bow shock region supports the hypothesis that the high-lying states of  $\text{H}_2$  observed on the HD 34078 sightline are produced in a hot layer near the star, swept-up by the passage of HD 34078, and excited by stellar UV photons.

The sightline to HD 34078 is seen to be highly reddened compared with other regions of IC 405 (France et al. 2004). This is inferred from the blue rise of the ratio of nebular surface brightness to stellar flux ( $S/F_*$ ) at far-UV wavelengths (900 – 1400 Å). The *Spitzer* data allow us to determine if this enhanced reddening can be attributed to the material associated with the shock region. Equation (6) of van Buren & McCray (1988) gives the UV optical depth ( $\tau_{UV}$ ) of the swept-up dust. Assuming that the majority of the dust survives the interaction with HD 34078 and that the swept-up material has a velocity of a few  $\text{km s}^{-1}$ ,  $\tau_{UV}$  is of the order 0.01. This relatively small value of  $\tau_{UV}$  is insufficient to explain the observed  $S/F_*$  in IC 405. In other words, the dust responsible for the differential extinction towards IC 405 is not associated with the bow shock. It is more likely that this dust is located in the translucent cloud along the HD 34078 sightline. This cloud is observed to produce the majority of the cold ( $J = 0, 1$ ;  $T(\text{H}_2) = 77$  K)  $\text{H}_2$  absorption (Boissé et al. 2005), and we conclude that this cloud is also responsible for the majority of the extinction towards HD 34078.

#### 4.2. $\text{H}_2$ and Dust Temperatures in Filaments A and B

Observationally, little attention has been paid to IC 405 in comparison with other bright PDRs (NGC 2023, NGC 7023, IC 63, and the Orion Bar). Here we establish the dust and  $\text{H}_2$  rotational temperatures of the outer filaments.

$H_2$  – Rotational temperatures can be measured from  $H_2$  emission line ratios in the IRS bandpass (Rosenthal et al. 2000; Allers et al. 2005). This temperature directly probes the bulk of the molecular mass in PDRs and has been a widely used diagnostic since a large number of mid-IR observations were made available by *ISO* (see references in the review by van Dishoeck 2004 and §1.1). We have used the IRS Short-Low measurements of the position averaged  $H_2$  S(3) and S(2) emission line strengths and Short-High observations of the central cores of Filaments A and B to determine  $T(H_2)$  for these regions. Only the brightest six Short-Low pointings corresponding to the ON position in Figures 10 and 12 were considered. The use of the Short-High module allows us to separate the (0–0) S(2)  $\lambda$ 12.28  $\mu$ m and S(1)  $\lambda$ 17.03  $\mu$ m lines from nearby spectral features. The S(2) and S(1) line strengths were measured from the two cleanest (defined as a combination of line S/N and a low, featureless background) Short-High observations at each filament. The S(2) and S(1) spectra from Filaments A and B are shown in Figure 15.

$T(H_2)$  was determined by combining the measured line ratios,  $I(S(2))/I(S(1))$  and  $I(S(3))/I(S(2))$ , with energy levels and transition probabilities from the literature. This temperature determination assumes that the pure rotational lines are optically thin and thermally populated, with an equilibrium ortho-to-para  $H_2$  ratio of 3. Internal and foreground attenuation is also assumed to be negligible, which is supported by the finding that the reddening towards the nebula is essentially zero at far-UV wavelengths (France et al. 2004).

The energy levels from Mandy & Martin (1993) give  $\Delta E_{21}/k = 667$  K, and the Einstein-A radiative tran-

sition probabilities are  $A_{S(2)} = 2.76 \times 10^{-9} \text{ s}^{-1}$  and  $A_{S(1)} = 4.76 \times 10^{-10} \text{ s}^{-1}$  (Wolniewicz et al. 1998). The ratio of level degeneracies,  $g_{S(2)}/g_{S(1)}$ , is 9/21. Using these parameters, we obtain rotational temperatures of  $T_{21}^A(H_2) = 692 \pm 55$  K and  $T_{21}^B(H_2) = 381 \pm 28$  K for Filaments A and B, respectively. These temperatures are higher than one would expect for a cold interstellar cloud, but are similar to recent PDR observations that find typical  $H_2$  rotational temperatures in the range of a few hundred degrees K (Thi et al. 1999; Habart et al. 2004; Allers et al. 2005).

Noting the added uncertainties in the continuum levels discussed above, we also calculated the  $H_2$  rotational temperature using position averaged strengths of the S(3) and S(2) lines observed in the low-dispersion spectra. Including the values for  $A_{S(3)}$ ,  $\Delta E_{32}/k$ , from the references given above with  $g_{S(3)}$ , we found  $T_{32}^A(H_2) = 418_{-73}^{+108}$  K and  $T_{32}^B(H_2) = 387_{-39}^{+46}$  K. The agreement at Filament B is remarkable (381 vs. 387), but the Filament A temperatures differ by almost 300 K.

We interpret variations seen at Filament A as differing relative populations in adjacent rotational states, indicative of the influence of non-thermal excitation by far-UV photons. The distribution of excited rovibrational states produced in the fluorescent cascade differs from a thermal distribution, and this is reflected in the observed emission line ratios (Black & van Dishoeck 1987). If the filament structure is clumpy, the narrower field-of-view of the Short-High aperture (as opposed to the position averaged Short-Low data used to determine  $T_{32}(H_2)$ ) could be dominated by a knot with a larger non-thermal emission fraction. Two tests of the Short-Low data have been performed to explore this possibility. We have used the individual  $H_2$  S(3) and S(2) line strengths to look at  $T_{32}$  as a function of position. This shows that the derived  $H_2$  rotational temperature displays excursions to greater than 700 K, albeit at the lower signal to noise positions not considered in the average line strengths used to determine  $T_{32}$  above. Secondly, we looked at temperature variations along the Short-Low slit at a pointing that spatially overlapped the Short-High spectra used. We measured a higher temperature ( $T_{32}^A(H_2) \gtrsim 520$  K) along the star-facing edge of Filament A, coincident with the Short-High positions, suggesting that the line ratios used to determine the  $H_2$  rotational temperature may be altered by UV photons in this region.

The majority of rovibrational emission lines that would indicate fluorescent pumping fall at wavelengths shorter than the *Spitzer*-IRS bandpass, thus IRS spectroscopy alone may not be sufficient to constrain the excitation mechanism of nebular  $H_2$ . In IC 405 however, direct evidence for non-thermal (fluorescent) excitation of  $H_2$  has been presented by France et al. (2004). *FUSE* observations clearly revealed the far-UV spectrum of fluorescent molecular hydrogen at Filaments A and B. These spectra are shown in Figure 16. Filament A is shown in the top panel, where the emission from  $H_2$  is seen imposed upon dust-scattered light from HD 34078. We note that the fluorescent lines at Pos3 display a broadening in excess of the instrumental width, as has been seen in the  $H_2$  emission spectra of other PDRs (France et al. 2005). HD 34078 is clearly identified as the excita-

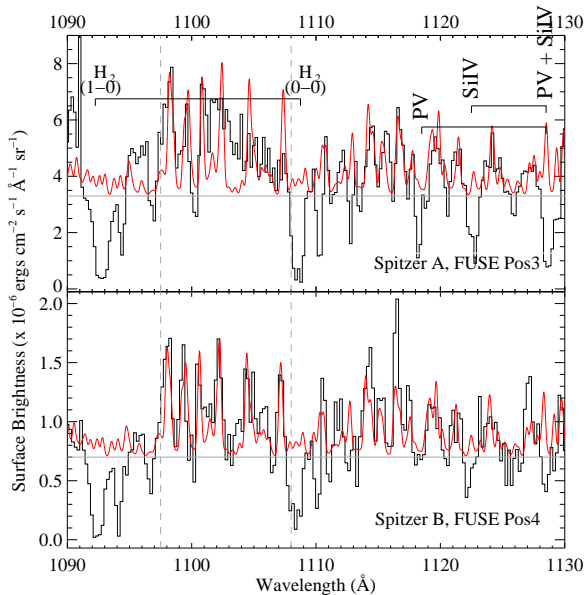


FIG. 16.— *FUSE* observations of Filaments A (above) and B (below).  $H_2$  fluorescence is observed at each position imposed on the dust scattered continuum of HD 34078, providing direct evidence for a population of photo-excited nebular gas. A synthetic spectrum of  $H_2$  emission, scaled to the flux level of the data, is overplotted. Lyman band  $H_2$  (labeled 0–0 and 1–0) and photo-spheric absorption lines are also observed.

tion source by the highly excited photospheric features of P V and Si IV seen in the scattered light. As has been shown for fluorescent H<sub>2</sub> emission near the Trapezium (France & McCandliss 2005), a star with such photospheric ions (Pellerin et al. 2002) is the most likely to have the requisite far-UV flux ( $\lambda \lesssim 1110 \text{ \AA}$ ) to produce observable UV fluorescence. The *FUSE* spectrum of Filament B is shown in the bottom panel, overplotted with a synthetic H<sub>2</sub> spectrum (France et al. 2004). It is interesting to note that the synthetic spectrum was created with a rotational temperature of 400 K, only attempting to find qualitative agreement with the data. The fluorescent H<sub>2</sub> was integrated over the strongest far-UV line complex (1097.7 – 1108.0 Å) after subtracting the contribution from dust scattered light. Integrated surface brightnesses are quoted in Table 5.

Fluorescent excitation by HD 34078 can also be observed in the highly excited H<sub>2</sub> absorption lines on the HD 34078 sightline (Boissé et al. 2005). As non-thermal emission clearly plays a role in IC 405, we propose that the average rotational temperatures of the filaments is  $\sim 400 \text{ K}$ , while UV-pumping has produced non-uniform excitation. The result of this excitation has been to alter the observed line ratios at the Short-High pointings used in Filament A, leading to the observed temperature deviation.

*Dust* – Thermal dust temperature ( $T_d$ ) can be determined from mid and far-IR photometry, made widely available by *IRAS* (Sodroski et al. 1987; Schnee et al. 2005). Measurements of  $T_d$  fit two or more IR data points, assuming emission from the dust cloud is described by a modified black-body curve. The black-body function is typically modified by a power-law emissivity function that is representative of the grain composition.

We have used the 24 and 70  $\mu\text{m}$  MIPS observations of IC 405 to derive the dust temperature in the three filaments where the scans overlap (A\*, A\*\*, and B), as well as across the bow shock region (§4.1.1). The contribution of discrete spectral features to the photometric flux in these bands has been considered. The weak spectral features in IRS Long-Low (20 – 30  $\mu\text{m}$ ) observations contribute less than  $\sim 8\%$  of the 24  $\mu\text{m}$  band flux at all pointings. The contribution of line emission to the 70  $\mu\text{m}$  brightness is more difficult to constrain without the aid of spectroscopy. We note that [O I]  $\lambda 63 \mu\text{m}$  lies at the edge of the MIPS 70  $\mu\text{m}$  filter. [O I] may be strong in IC 405 (van Dishoeck 2004), but without direct measurement of the nebular SED at these wavelengths, we do not attempt to correct for emission lines.

The observed  $F_{24}/F_{70}$  photometric ratio, computed from Tables 3 and 4, was fit using a modified black body spectrum, with a dust emissivity proportional to  $\nu^2$ . The choice for the dust emissivity law was determined by the theoretical dust absorption opacity wavelength dependence  $2.92 \times 10^5 (\lambda/\mu\text{m})^{-2}$ , valid in the  $20 \mu\text{m} \leq \lambda \leq 700 \mu\text{m}$  range for the average diffuse ISM (Li & Draine 2001). The spectral slope in the 24 and 70  $\mu\text{m}$  filter bandpasses does not make a significant contribution to the resulting brightness ratios, the correction being significantly smaller than our measurement errors for  $T_d \geq 40 \text{ K}$ .

The  $F_{24}/F_{70}$  ratios were nearly identical in the three filaments, 0.379 (§3.1), and the inferred dust tempera-

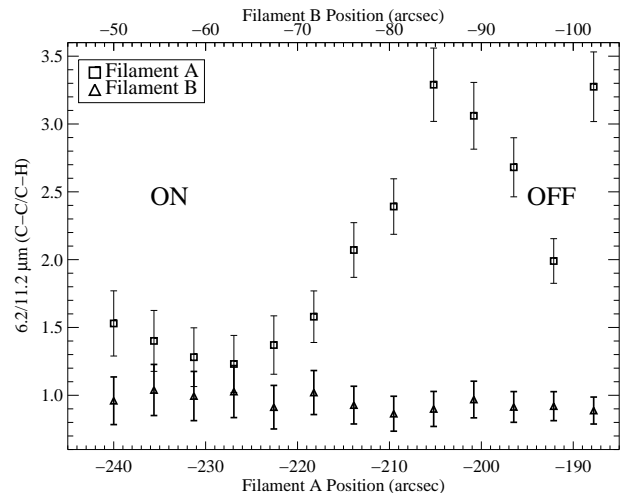


FIG. 17.— IRS measurements of the ratio of 6.2 and 11.2  $\mu\text{m}$  line strengths in Filaments A and B. Their ratio is an indication of the ionization state of the aromatics in these regions. The relative ionization fraction increases off the core of Filament A, but is seen to be constant at Filament B. *Note* : The Filament B data is displayed ON (-50'') to OFF (-105'') for comparison with Filament A in this plot.

tures reflect this. The mean temperature for the nebular dust in IC 405 is 63 K. Individually, the observed filament dust temperatures are  $T_d^{A^*} = 62.8 \pm 1.5$ ,  $T_d^{A^{**}} = 62.6 \pm 1.4$ , and  $T_d^B = 62.7 \pm 1.6 \text{ K}$ . These grain temperatures are roughly a factor of 3.5 higher than those found for molecular clouds in Perseus, Ophiucus, and Serpens ( $\langle T_d \rangle = 17 \text{ K}$ ; Schnee et al. 2005), suggesting that the grains have processed the UV photons from HD 34078. Our derived temperature for the IC 405 filaments is similar to the lower limit of the dust temperature (55 K) in the Orion Bar PDR (Lis et al. 1998). What may be surprising about the IC 405 dust measurements is the similarity of the temperature at Filaments A\* and A\*\* (roughly equidistant from HD 34078) with that of Filament B. Single photon heating effects should be important for grains with  $\lesssim 1000$  carbon atoms in the intense radiation field of HD 34078 (Draine & Li 2001). This may be the cause of the constant temperature distribution in the nebular filaments.

#### 4.3. Ionization and Molecular Environment

There is general consensus that the AEFs are produced by a superposition of vibrational modes of large carbonaceous molecules (Verstraete et al. 2001; Peeters et al. 2002). Laboratory and theoretical studies have shown that the typical interstellar aromatic emission spectrum is composed of a combination of neutral and ionized carriers with a distribution of sizes (see the review by van Dishoeck, 2004, and references therein). These studies have shown that cations (positively charged ions) have enhanced 6 – 10  $\mu\text{m}$  features arising from stronger C – C stretching modes. Neutral molecules have stronger C – H bands, producing the majority of the aromatic emission at 3.3 and 10 – 14  $\mu\text{m}$  (Hony et al. 2001; Bregman & Temi 2005). The ratio of 6.2/11.2  $\mu\text{m}$  emission bands can be indicators of ionization (Uchida et al. 2000; Bakes et al. 2001) and molec-

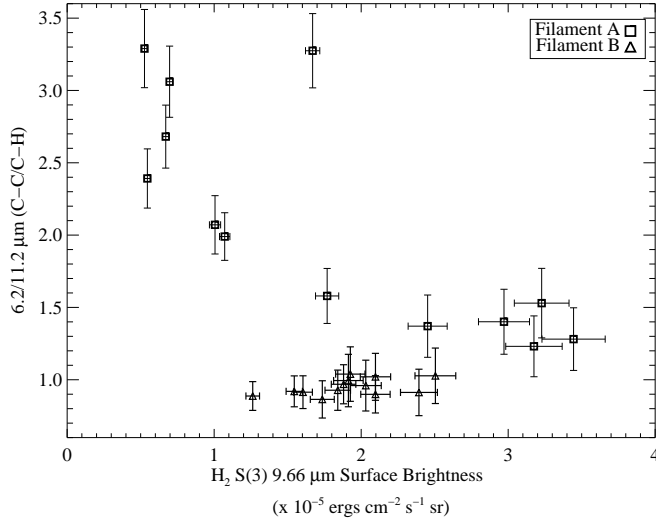


FIG. 18.— The ionization measure of the AEF carriers ( $6.2/11.2 \mu\text{m}$ ) as a function of strength of the molecular hydrogen emission at  $9.66 \mu\text{m}$ . The correlation observed at Filament A suggests that ionization of the aromatics increases in lower density environments at given radiation field (Bakes et al. 2001). No trend is observed at Filament B.

ular structure (Chan et al. 2001; Hony et al. 2001).

IRS scans of the two filaments in IC 405 allow us to study the change in ionization state with environment. Assuming that Filaments A and B are located at roughly the same heliocentric distance as HD 34078, we can constrain the relative radiation fields at the two positions. Variations in the spectral properties along Filaments A and B can be correlated with change in filament structure/density *and* changing radiation field. Previous studies have primarily focused on the variations of AEFs with radiation field strength (Verstraete et al. 1996; Peeters et al. 2002; Werner et al. 2004b). Our results for molecular ionization fraction as a function of position are shown in Figure 17. The scan moves off the filament to the right, the position coordinates have been calculated to correspond to the images presented in this work. The  $6.2/11.2$  ratio is displayed as squares for Filament A and triangles for Filament B. We observed an increase in ionization fraction as the scan moves from the central knot to the diffuse nebula at Filament A, going from roughly 1.4 to 3.3. This can be understood as an increase in the contribution from ionized carriers in less dense regions at a constant radiation field (Bakes et al. 2001).

The ionization fraction is seen to be constant with position in Filament B. The baseline  $6.2/11.2 \mu\text{m}$  ratio is lower in Filament B than in Filament A ( $\sim 0.9$  vs  $1.4$ ), suggesting that the overall ionization fraction is smaller in Filament B. Filament B is roughly twice the angular distance from HD 34078 and consequently receives about a quarter of the UV flux present at Filament A, consistent with the *FUSE* observations presented in §4.2. While the ionization fraction declines with diminishing UV flux, there might not be a one-to-one relationship. This conclusion is derived in connection to the assertion made in §3.3 that Filament A shows indirect evidence

for enhanced AEF carrier destruction relative to Filament B. Using the Filament B region as a baseline, our observations are consistent with the photodestruction of the aromatic molecules responsible for the AEFs being a multi-step process where dissociation is preceded by ionization. Additional observations of PDRs are available in the *Spitzer* and *ISO* archives, and we will explore similarities with IC 405 in future work.

The AEF ionization measure can also be correlated with the environment in which  $\text{H}_2$  emission is produced. A comparison of the  $\text{H}_2$  emission strength and AEF ionization is shown in Figure 18. The S(3) rotational line was used as representative of  $\text{H}_2$  emission because of its brightness and separation from other lines. We observe the AEF ionization fraction to increase as the molecular hydrogen line strength decreases in Filament A. Assuming that  $\text{H}_2$  is representative of density, these results also indicate that the AEF carrier population is more ionized in more tenuous regions at a given UV radiation field (Bakes et al. 2001). Combining this result with the spatial dependence of the molecular ionization described above confirm that in strongly illuminated PDRs, the  $6.2/11.2 \mu\text{m}$  ratio is a good diagnostic of the local ionization conditions. This result is consistent with the Bakes et al. (2001) prediction for regions with a ratio of ionizing radiation field to electron density ( $G_0/n_e$ ) of  $\sim 10^4 \text{ cm}^3$ . No correlation is observed at Filament B.

#### 4.4. Substructure in the $6.2 \mu\text{m}$ Feature – Evidence for PANHs?

In addition to providing information about the ionization state, the  $6.2 \mu\text{m}$  feature can be a diagnostic of the AEF carrier structure. Peeters et al. (2002) have performed a survey of the  $6.2 \mu\text{m}$  feature in a variety of astronomical objects, and have determined empirical subclasses for this band. Lines with peak wavelengths near  $6.22 \mu\text{m}$  form Class A, while lines peaking between  $6.24$  and  $6.3 \mu\text{m}$  make up Classes B and C. Most H II regions, reflection nebulae, and non-isolated Herbig Ae/Be stars belong to Class A, while isolated Herbig Ae/Be stars and most planetary nebulae belong to Class B. They find red-peaked ( $\lambda_o \sim 6.3 \mu\text{m}$ ) lines to be composed of “pure” PAHs, while blue-peaked ( $\lambda_o \sim 6.2 \mu\text{m}$ ) lines have N-atoms substituted at inner lattice sites.

Hudgins et al. (2005) carry the nitrogenation hypothesis further, determining the necessary site for N-substitution in order to reproduce the observed  $6.2 \mu\text{m}$  wavelength and ruling out increasing molecular size alone as the explanation for the observed line profiles. They find that nitrogen substitution is required to reproduce the observed profiles, labeling this PAH subclass polycyclic aromatic nitrogen heterocycles (PANHs). They conclude that PAHs or PANHs with N-substitution on the edges of the molecule produce the emission at  $\lambda \geq 6.3 \mu\text{m}$ , while PANHs with the N-atom substituted in the interior of the molecule are responsible for the Class A spectra observed by Peeters et al. (2002).

With this observational and theoretical evidence in mind, we report a tentative detection of band substructure to the red of the main  $6.2 \mu\text{m}$  peak at Filament A. Filament A spectra are shown in Figure 19 from  $5.8 - 7.2 \mu\text{m}$ . The spectra are dominated by a main Class A feature at  $\lambda_{max} = 6.210 \pm 0.007 \mu\text{m}$ . At the peak filament brightness position, we observe an enhanced red

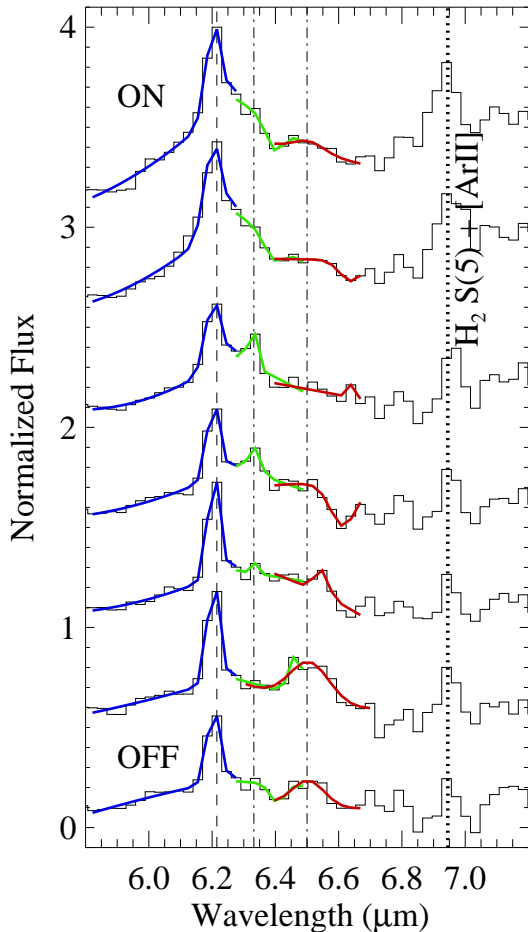


FIG. 19.— IRS Short-Low observations of the  $6.2 \mu\text{m}$  AEF in Filament A. The spectra have been normalized to the peak of the on-filament  $6.2 \mu\text{m}$  band and offset by factors of 0.5 for this display. The data show a variation in the  $6.2 \mu\text{m}$  profile from the core of the filament (ON, top) to the edges (OFF, bottom). The spectra maintain a Class A  $6.2 \mu\text{m}$  peak (Peeters et al. 2002), but develop red substructure away from the core of the filament. Three Gaussians are fitted to the spectra showing the main peak (blue), the second peak seen at  $6.33 \mu\text{m}$  (green), and the broad  $6.5 \mu\text{m}$  “hump” (red). The  $6.5 \mu\text{m}$  Gaussian on the second OFF spectrum (offset = +0.5) was fit over a slightly expanded wavelength range to show the feature more clearly.

wing to the main feature. This wing develops a distinct second peak at  $6.33 \mu\text{m}$  as the overall  $6.2 \mu\text{m}$  band decreases in strength away from the central core of the filament. An additional red “hump” appears further to the red ( $\lambda \sim 6.50 \mu\text{m}$ ) becoming stronger with increasing distance from the peak filament brightness position. Three Gaussians are shown overplotted on the data in Figure 18 representing each component. The  $\text{H}_2 + [\text{Ar II}]$  blend is seen near  $6.95 \mu\text{m}$ .

The red features are qualitatively similar to the coronene cation ( $\text{C}_{24}\text{H}_{12}^+$ ) spectra shown in Figure 3 of Hudgins et al. (2005). The substructure is most pronounced in the same region where the ionization fraction is seen to increase. One interpretation is that processing by UV photons is altering the PAH population in

the interface between the dense filament and the more tenuous nebular regions. We only see red substructure in one Filament B spectrum. Filament B is generally observed to have an unmodified Class A  $6.2 \mu\text{m}$  band,  $\lambda_{\text{max}} = 6.219 \pm 0.004 \mu\text{m}$ . We note that a  $6.35 \mu\text{m}$  feature was reported as a red shoulder of the  $6.2 \mu\text{m}$  band in *ISO* observations of M17–SW (Verstraete et al. 1996), interpreted as large PAHs under the influence of a strong UV radiation field. However, Peeters et al. (2002) report no detection of a  $6.35 \mu\text{m}$  feature.

## 5. SUMMARY

We have presented new *Spitzer* observation of IC 405, an emission/reflection nebula in Auriga illuminated by the runaway O9.5 star HD 34078. We have used IRS spectroscopy to assess the morphological differences seen in four band ( $3.6, 4.5, 5.8,$  and  $8.0 \mu\text{m}$ ) imaging obtained with IRAC. The combination of the IRAC data with  $24$  and  $70 \mu\text{m}$  MIPS maps of the nebula reveal wavelength dependent morphology in several subregions. We attribute these differences to variations in the relative strengths of AEFs and emission from grains. In addition to the AEFs, the spectroscopy revealed emission from the pure rotational lines of  $\text{H}_2$  and atomic fine structure lines. The emission bands/lines were observed to vary in both absolute and relative strength as a function of position at two bright nebular filaments.

Dust temperatures in three nebular filaments were derived from  $24$  and  $70 \mu\text{m}$  photometry. The dust temperature was a constant  $63 \text{ K}$ , independent of the distance from the illuminating star. A similar temperature analysis performed on spatial profiles of the  $24$  and  $70 \mu\text{m}$  data obtained near HD 34078 show elevated dust temperatures ( $\gtrsim 90 \text{ K}$ ) in a bow shock ahead of the star, in the direction of stellar motion. The bow shock scenario is supported by the cometary morphological structure seen in the  $8.0$  and  $24 \mu\text{m}$  images of the stellar region. We use this data to support the two-component model for the HD 34078 sightline. The excited  $\text{H}_2$  is thought to be associated with the shock region, while the majority of the cold  $\text{H}_2$  absorption and dust extinction occurs in an intervening translucent cloud.

The measured AEF line strength were found to be anticorrelated with the intensity of the far-UV radiation field in the nebula, possibly due to increased destruction of the aromatics. The spectroscopic data also were used to constrain the relative ionization state of the AEF carrier molecules. The ionization state was seen to increase with decreasing density in one filament. This ionization fraction was seen to be anticorrelated with the  $\text{H}_2$  emission line strength, consistent with enhanced AEF carrier ionization with decreasing density at a given UV radiation field. Evidence was presented for substructure in the  $6.2 \mu\text{m}$  AEF, suggestive of changing carrier size and/or composition as a function of nebular environment. Line ratios were used to derive the  $\text{H}_2$  rotational temperature in two filaments, indicating an average rotational temperature of roughly  $400 \text{ K}$ , with evidence for additional non-uniform excitation in the filament nearer to the illuminating star. These measurements were complemented by observations of the far-UV  $\text{H}_2$  fluorescence spectrum, providing direct evidence for excitation by UV photons.

As new imaging and spectroscopic observations of PDRs become available in the *Spitzer* archive, oppor-

tunities for comparative studies with existing UV data are made possible. Combining the UV and mid-IR observations with near-IR observations of the rovibrational emission lines of H<sub>2</sub>, an accounting of the energy redistribution following electronic excitation can be carried out in order to test models of H<sub>2</sub> fluorescence. A panchromatic H<sub>2</sub> spectrum could be produced in a variety of PDRs, from pure reflection nebulae (NGC 2023) to star-forming regions (Orion Bar) to H II regions with harder radiation fields (planetary nebulae such as M 27). These data would allow models that span a wide range in excitation temperature, density, and radiation field to be compared with observation. H<sub>2</sub> observations can be compared to the AEF and dust properties in these regions in order to explore the relationship between molecular-phase PDR diagnostics and local environmental charac-

teristics.

It is a pleasure to acknowledge B-G Andersson for several discussions about the infrared properties of dust grains. We thank an anonymous referee, whose comments greatly improved the quality of this paper. This work is based in part on observations made with the *Spitzer Space Telescope*, which is operated by the Jet Propulsion Laboratory, California Institute of Technology under a contract with NASA. Support for this work was provided by JPL grant JPL1276492 to The Johns Hopkins University. The *FUSE* data were obtained under the Guest Investigator Program of the NASA-CNES-CSA *FUSE* mission, operated by The Johns Hopkins University.

## REFERENCES

- Abel, N. P., Ferland, G. J., Shaw, G., & van Hoof, P. A. M. 2005, *ApJS*, 161, 65
- Allers, K. N., Jaffe, D. T., Lacy, J. H., Draine, B. T., & Richter, M. J. 2005, *ApJ*, 630, 368
- Armus, L., Charmandaris, V., Spoon, H. W. W., Houck, J. R., Soifer, B. T., Brandl, B. R., Appleton, P. N., Teplitz, H. I., Higdon, S. J. U., Weedman, D. W., Devost, D., Morris, P. W., Uchida, K. I., van Cleve, J., Barry, D. J., Sloan, G. C., Grillmair, C. J., Burgdorf, M. J., Fajardo-Acosta, S. B., Ingalls, J. G., Higdon, J., Hao, L., Bernard-Salas, J., Herter, T., Troeltzsch, J., Unruh, B., & Winghart, M. 2004, *ApJS*, 154, 178
- Bagnuolo, Jr., W. G., Riddle, R. L., Gies, D. R., & Barry, D. J. 2001, *ApJ*, 554, 362
- Bakes, E. L. O., Tielens, A. G. G. M., & Bauschlicher, Jr., C. W. 2001, *ApJ*, 556, 501
- Blaauw, A. & Morgan, W. W. 1954, *ApJ*, 119, 625
- Black, J. H. & van Dishoeck, E. F. 1987, *ApJ*, 322, 412
- Boissé, P., Le Petit, F., Rollinde, E., Roueff, E., Pineau des Forêts, G., Andersson, B.-G., Gry, C., & Felenbok, P. 2005, *A&A*, 429, 509
- Boulanger, F., Abergel, A., Cesarsky, D., Bernard, J. P., Miville Deschênes, M. A., Verstraete, L., & Reach, W. T. 2000, in *ESA SP-455: ISO Beyond Point Sources: Studies of Extended Infrared Emission*, ed. R. J. Laureijs, K. Leech, & M. F. Kessler, 91–
- Bregman, J. & Temi, P. 2005, *ApJ*, 621, 831
- Bregman, J. D., Allamandola, L. J., Witteborn, F. C., Tielens, A. G. G. M., & Geballe, T. R. 1989, *ApJ*, 344, 791
- Burgh, E. B., McCandliss, S. R., & Feldman, P. D. 2002, *ApJ*, 575, 240
- Cardelli, J. A., Clayton, G. C., & Mathis, J. S. 1989, *ApJ*, 345, 245
- Cazaux, S. & Tielens, A. G. G. M. 2002, *ApJ*, 575, L29
- . 2004, *ApJ*, 604, 222
- Cesarsky, D., Lequeux, J., Ryter, C., & Gérin, M. 2000, *A&A*, 354, L87
- Chan, K.-W., Roellig, T. L., Onaka, T., Mizutani, M., Okumura, K., Yamamura, I., Tanabé, T., Shibai, H., Nakagawa, T., & Okuda, H. 2001, *ApJ*, 546, 273
- Cohen, M., Tielens, A. G. G. M., & Allamandola, L. J. 1985, *ApJ*, 299, L93
- Draine, B. T. 2003, *ApJ*, 598, 1017
- Draine, B. T. & Li, A. 2001, *ApJ*, 551, 807
- Draine, B. T., Roberge, W. G., & Dalgarno, A. 1983, *ApJ*, 264, 485
- Fazio, G. G., Hora, J. L., Allen, L. E., Ashby, M. L. N., Barmby, P., Deutsch, L. K., Huang, J.-S., Kleiner, S., Marengo, M., Megeath, S. T., Melnick, G. J., Pahre, M. A., Patten, B. M., Polizotti, J., Smith, H. A., Taylor, R. S., Wang, Z., Willner, S. P., Hoffmann, W. F., Pipher, J. L., Forrest, W. J., McMurty, C. W., McCreight, C. R., McKelvey, M. E., McMurray, R. E., Koch, D. G., Moseley, S. H., Arendt, R. G., Mentzell, J. E., Marx, C. T., Losch, P., Mayman, P., Eichhorn, W., Krebs, D., Jhabvala, M., Gezari, D. Y., Fixsen, D. J., Flores, J., Shakoorzadeh, K., Jungo, R., Hakun, C., Workman, L., Karpati, G., Kichak, R., Whitley, R., Mann, S., Tollestrup, E. V., Eisenhardt, P., Stern, D., Gorjian, V., Bhattacharya, B., Carey, S., Nelson, B. O., Glaccum, W. J., Lacy, M., Lowrance, P. J., Laine, S., Reach, W. T., Stauffer, J. A., Surace, J. A., Wilson, G., Wright, E. L., Hoffman, A., Domingo, G., & Cohen, M. 2004, *ApJS*, 154, 10
- France, K., Andersson, B.-G., McCandliss, S. R., & Feldman, P. D. 2005, *ApJ*, 628, 750
- France, K. & McCandliss, S. R. 2005, *ApJ*, 629, L97
- France, K., McCandliss, S. R., Burgh, E. B., & Feldman, P. D. 2004, *ApJ*, 616, 257
- Gordon, K., Englebracht, C., Smith, J., Rieke, G., & Misselt, K. 2006, *astro-ph*, 0605544
- Habart, E., Boulanger, F., Verstraete, L., Walmsley, C. M., & Pineau des Forêts, G. 2004, *A&A*, 414, 531
- Heitsch, R., Whitney, B. A., Indebetow, R., Meade, M. R., Babler, B. L., & Churchwell, E. 2006, *ApJ*, *astro-ph*0607318
- Herbig, G. H. 1958, *PASP*, 70, 468
- . 1999, *PASP*, 111, 809
- Hollenbach, D. & Tielens, A. 1997, *Annual Reviews of Astronomy and Astrophysics*, 35, 179
- Hony, S., Van Kerckhoven, C., Peeters, E., Tielens, A. G. G. M., Hudgins, D. M., & Allamandola, L. J. 2001, *A&A*, 370, 1030
- Hora, J., Latter, W. B., Smith, H., & Marengo, M. 2006, *ApJ*, *astro-ph*0607541
- Houck, J. R., Roellig, T. L., van Cleve, J., Forrest, W. J., Herter, T., Lawrence, C. R., Matthews, K., Reitsema, H. J., Soifer, B. T., Watson, D. M., Weedman, D., Huisjen, M., Troeltzsch, J., Barry, D. J., Bernard-Salas, J., Blacken, C. E., Brandl, B. R., Charmandaris, V., Devost, D., Gull, G. E., Hall, P., Henderson, C. P., Higdon, S. J. U., Pirger, B. E., Schoenwald, J., Sloan, G. C., Uchida, K. I., Appleton, P. N., Armus, L., Burgdorf, M. J., Fajardo-Acosta, S. B., Grillmair, C. J., Ingalls, J. G., Morris, P. W., & Teplitz, H. I. 2004, *ApJS*, 154, 18
- Hudgins, D. M., Bauschlicher, Jr., C. W., & Allamandola, L. J. 2005, *ApJ*, 632, 316
- Huggins, P. J., Forveille, T., Bachiller, R., Cox, P., Ageorges, N., & Walsh, J. R. 2002, *ApJ*, 573, L55
- Hurwitz, M. 1998, *ApJ*, 500, L67+
- Huthoff, F. & Kaper, L. 2002, *A&A*, 383, 999
- Jansen, D. J., van Dishoeck, E. F., & Black, J. H. 1994, *A&A*, 282, 605
- Jansen, D. J., van Dishoeck, E. F., Black, J. H., Spaans, M., & Sosin, C. 1995, *A&A*, 302, 223
- Kastner, J. H., Weintraub, D. A., Gatley, I., Merrill, K. M., & Probst, R. G. 1996, *ApJ*, 462, 777

- Kristensen, L. E., Gustafsson, M., Field, D., Callejo, G., Lemaire, J. L., Vannier, L., & Pineau des Forêts, G. 2003, *A&A*, 412, 727
- Li, A. & Draine, B. T. 2001, *ApJ*, 554, 778
- Lis, D. C., Serabyn, E., Keene, J., Dowell, C. D., Benford, D. J., Phillips, T. G., Hunter, T. R., & Wang, N. 1998, *ApJ*, 509, 299
- Luhman, M. L. & Jaffe, D. T. 1996, *ApJ*, 463, 191
- Luhman, M. L., Luhman, K. L., Benedict, T., Jaffe, D. T., & Fischer, J. 1997, *ApJ*, 480, L133+
- Lupu, R. E., France, K., & McCandliss, S. R. 2006, *ApJ*, 644, 981
- Mac Low, M.-M., van Buren, D., Wood, D. O. S., & Churchwell, E. 1991, *ApJ*, 369, 395
- Mandy, M. E. & Martin, P. G. 1993, *ApJS*, 86, 199
- Martini, P., Sellgren, K., & DePoy, D. L. 1999, *ApJ*, 526, 772
- Martins, F., Schaerer, D., Hillier, D. J., Meynadier, F., Heydari-Malayeri, M., & Walborn, N. R. 2005, *A&A*, 441, 735
- Moos, H. W. e. a. 2000, *ApJ*, 538, L1
- Noriega-Crespo, A., van Buren, D., & Dgani, R. 1997, *AJ*, 113, 780
- Peeters, E., Hony, S., Van Kerckhoven, C., Tielens, A. G. G. M., Allamandola, L. J., Hudgins, D. M., & Bauschlicher, C. W. 2002, *A&A*, 390, 1089
- Peeters, E., Mattioli, A. L., Hudgins, D. M., & Allamandola, L. J. 2004, *ApJ*, 617, L65
- Pellierin, A., Fullerton, A. W., Robert, C., Howk, J. C., Hutchings, J. B., Walborn, N. R., Bianchi, L., Crowther, P. A., & Sonneborn, G. 2002, *ApJS*, 143, 159
- Poglitsch, A., Waelkens, C., Bauer, O. H., Cepa, J., Henning, T. F., van Hoof, C., Katterloher, R., Kerschbaum, F., Lemke, D., Renotte, E., Rodriguez, L., Royer, P., & Saraceno, P. 2004, in *Microwave and Terahertz Photonics*. Edited by Stohr, Andreas; Jager, Dieter; Iezekiel, Stavros. *Proceedings of the SPIE*, Volume 5487, pp. 425-436 (2004)., ed. J. C. Mather, 425-436
- Rieke, G. H., Young, E. T., Engelbracht, C. W., Kelly, D. M., Low, F. J., Haller, E. E., Beeman, J. W., Gordon, K. D., Stansberry, J. A., Misselt, K. A., Cadien, J., Morrison, J. E., Rivlis, G., Latter, W. B., Noriega-Crespo, A., Padgett, D. L., Stapelfeldt, K. R., Hines, D. C., Egami, E., Muzerolle, J., Alonso-Herrero, A., Blaylock, M., Dole, H., Hinz, J. L., Le Floc'h, E., Papovich, C., Pérez-González, P. G., Smith, P. S., Su, K. Y. L., Bennett, L., Frayer, D. T., Henderson, D., Lu, N., Masci, F., Pesenson, M., Rebull, L., Rho, J., Keene, J., Stolovy, S., Wachter, S., Wheaton, W., Werner, M. W., & Richards, P. L. 2004, *ApJS*, 154, 25
- Rollinde, E., Boissé, P., Federman, S. R., & Pan, K. 2003, *A&A*, 401, 215
- Rosenthal, D., Bertoldi, F., & Drapatz, S. 2000, *A&A*, 356, 705
- Schnee, S. L., Ridge, N. A., Goodman, A. A., & Li, J. G. 2005, *ApJ*, 634, 442
- Schutte, W. A., Tielens, A. G. G. M., & Allamandola, L. J. 1993, *ApJ*, 415, 397
- Shaw, G., Ferland, G. J., Abel, N. P., Stancil, P. C., & van Hoof, P. A. M. 2005, *ApJ*, 624, 794
- Shull, M. & Beckwith, S. 1982, *Annual Reviews of Astronomy and Astrophysics*, 30, 163
- Sodroski, T. J., Dwek, E., Hauser, M. G., & Kerr, F. J. 1987, *ApJ*, 322, 101
- Speck, A. K., Meixner, M., Jacoby, G. H., & Knezek, P. M. 2003, *PASP*, 115, 170
- Stecher, T. P. & Williams, D. A. 1967, *ApJ*, 149, L29+
- Takami, M., Usuda, T., Sugai, H., Kawabata, H., Suto, H., & Tanaka, M. 2000, *ApJ*, 529, 268
- Thi, W. F., van Dishoeck, E. F., Black, J. H., Jansen, D. J., Evans, N. J., & Jaffe, D. T. 1999, in *ESA SP-427: The Universe as Seen by ISO*, ed. P. Cox & M. Kessler, 529+
- Uchida, K. I., Sellgren, K., Werner, M. W., & Houdashelt, M. L. 2000, *ApJ*, 530, 817
- Valentijn, E. A. & van der Werf, P. P. 1999, *ApJ*, 522, L29
- van Buren, D., Mac Low, M.-M., Wood, D. O. S., & Churchwell, E. 1990, *ApJ*, 353, 570
- van Buren, D. & McCray, R. 1988, *ApJ*, 329, L93
- van Buren, D., Noriega-Crespo, A., & Dgani, R. 1995, *AJ*, 110, 2914
- van Dishoeck, E. F. 2004, *ARA&A*, 42, 119
- Verstraete, L., Pech, C., Moutou, C., Sellgren, K., Wright, C. M., Giard, M., Léger, A., Timmermann, R., & Drapatz, S. 2001, *A&A*, 372, 981
- Verstraete, L., Puget, J. L., Falgarone, E., Drapatz, S., Wright, C. M., & Timmermann, R. 1996, *A&A*, 315, L337
- Werner, M. W., Roellig, T. L., Low, F. J., Rieke, G. H., Rieke, M., Hoffmann, W. F., Young, E., Houck, J. R., Brandl, B., Fazio, G. G., Hora, J. L., Gehrz, R. D., Helou, G., Soifer, B. T., Stauffer, J., Keene, J., Eisenhardt, P., Gallagher, D., Gautier, T. N., Irace, W., Lawrence, C. R., Simmons, L., Van Cleve, J. E., Jura, M., Wright, E. L., & Cruikshank, D. P. 2004a, *ApJS*, 154, 1
- Werner, M. W., Uchida, K. I., Sellgren, K., Marengo, M., Gordon, K. D., Morris, P. W., Houck, J. R., & Stansberry, J. A. 2004b, *ApJS*, 154, 309
- Witt, A. N., Petersohn, J. K., Holberg, J. B., Murthy, J., Dring, A., & Henry, R. C. 1993, *ApJ*, 410, 714
- Witt, A. N., Stecher, T. P., Boroson, T. A., & Bohlin, R. C. 1989, *ApJ*, 336, L21
- Wolniewicz, L., Simbotin, I., & Dalgarno, A. 1998, *ApJS*, 115, 293